

AEDC-TR-80-20

c.7

DOC NUM SER CN  
UNC03651-PDC A 1

# Laser-Raman/Rayleigh Flow Diagnostic Techniques Applied to Subsonic Flow

W. D. Williams, D. W. Sinclair, and L. L. Price  
ARO, Inc.

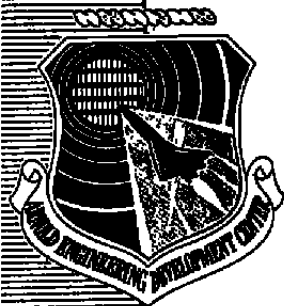
October 1980

Final Report for Period April 13, 1977 – March 14, 1978

Approved for public release; distribution unlimited.

Property of U. S. Air Force  
AEDC LIBRARY  
F40600-81-C-0004

**ARNOLD ENGINEERING DEVELOPMENT CENTER  
ARNOLD AIR FORCE STATION, TENNESSEE  
AIR FORCE SYSTEMS COMMAND  
UNITED STATES AIR FORCE**



## NOTICES

When U. S. Government drawings, specifications, or other data are used for any purpose other than a definitely related Government procurement operation, the Government thereby incurs no responsibility nor any obligation whatsoever, and the fact that the Government may have formulated, furnished, or in any way supplied the said drawings, specifications, or other data, is not to be regarded by implication or otherwise, or in any manner licensing the holder or any other person or corporation, or conveying any rights or permission to manufacture, use, or sell any patented invention that may in any way be related thereto.

Qualified users may obtain copies of this report from the Defense Technical Information Center.

References to named commercial products in this report are not to be considered in any sense as an indorsement of the product by the United States Air Force or the Government.

This report has been reviewed by the Office of Public Affairs (PA) and is releasable to the National Technical Information Service (NTIS). At NTIS, it will be available to the general public, including foreign nations.

## APPROVAL STATEMENT

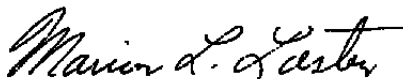
This report has been reviewed and approved.



KENNETH H. LENERS, Captain, USAF  
Project Manager  
Directorate of Technology

Approved for publication:

FOR THE COMMANDER



MARION L. LASTER  
Director of Technology  
Deputy for Operations

# UNCLASSIFIED

REPORT DOCUMENTATION PAGE		READ INSTRUCTIONS BEFORE COMPLETING FORM
1. REPORT NUMBER <b>AEDC-TR-80-20</b>	2. GOVT ACCESSION NO.	3. RECIPIENT'S CATALOG NUMBER
4. TITLE (and Subtitle) <b>LASER-RAMAN/RAYLEIGH FLOW DIAGNOSTIC TECHNIQUES APPLIED TO SUBSONIC FLOW</b>		5. TYPE OF REPORT & PERIOD COVERED <b>Final Report, April 13, 1977 - March 14, 1978</b>
		6. PERFORMING ORG. REPORT NUMBER
7. AUTHOR(s) <b>W. D. Williams, D. W. Sinclair, and L. L. Price, ARO, Inc., a Sverdrup Corporation Company</b>		8. CONTRACT OR GRANT NUMBER(s)
9. PERFORMING ORGANIZATION NAME AND ADDRESS <b>Arnold Engineering Development Center/DOT Air Force Systems Command Arnold Air Force Station, TN 37389</b>		10. PROGRAM ELEMENT, PROJECT, TASK AREA & WORK UNIT NUMBERS <b>Program Element 65807F</b>
11. CONTROLLING OFFICE NAME AND ADDRESS <b>Arnold Engineering Development Center/DOS Air Force Systems Command Arnold Air Force Station, TN 37389</b>		12. REPORT DATE <b>October 1980</b>
		13. NUMBER OF PAGES <b>54</b>
14. MONITORING AGENCY NAME & ADDRESS (if different from Controlling Office)		15. SECURITY CLASS. (of this report)  <b>UNCLASSIFIED</b>
		15a. DECLASSIFICATION DOWNGRADING SCHEDULE <b>N/A</b>
16. DISTRIBUTION STATEMENT (of this Report)  <b>Approved for public release; distribution unlimited.</b>		
17. DISTRIBUTION STATEMENT (of the abstract entered in Block 20, if different from Report)		
18. SUPPLEMENTARY NOTES  <b>Available in Defense Technical Information Center (DTIC).</b>		
19. KEY WORDS (Continue on reverse side if necessary and identify by block number) <b>flow-field measurements hypersonic flow Raman spectroscopy Raman/Rayleigh scattering</b>		
20. ABSTRACT (Continue on reverse side if necessary and identify by block number) <b>The feasibility of performing laser-Raman/Rayleigh scattering measurements in subsonic flows was demonstrated in the 6-in. Acoustic Research Tunnel (ART) of the Propulsion Wind Tunnel facility at AEDC. The ART is an open-circuit, atmospheric inbleed tunnel that operates on the Plenum Evacuation System of the 16-ft transonic Propulsion Wind Tunnel (16T). Laser-Raman/Rayleigh scattering techniques were used to measure air number density, H<sub>2</sub>O number density, and static temperature and to detect the onset of water</b>		

# UNCLASSIFIED

# UNCLASSIFIED

## 20. ABSTRACT, Concluded.

vapor condensation. Measurements were made near the tunnel axial centerline over the Mach number range from 0.10 to 0.80. Measurements were also made in the turbulent boundary layer on the wall of the test section at Mach numbers 0.50 to 0.80.

UNCLASSIFIED

## **PREFACE**

The work reported herein was conducted by the Arnold Engineering Development Center (AEDC), Air Force Systems Command (AFSC). The results of the research were obtained by ARO, Inc., AEDC Group (a Sverdrup Corporation Company), operating contractor for the AEDC, AFSC, Arnold Air Force Station, Tennessee, under ARO Project Numbers V32I-A1A, V32I-PIA, P32A-G6A, and P32S-R6A. Captain Stanislaus L. Ludwig (CF) was the AEDC project manager. The data analysis was completed on June 18, 1978, and the manuscript was submitted for publication on April 11, 1980.

## CONTENTS

	<u>Page</u>
1.0 INTRODUCTION .....	5
2.0 THEORY OF RAMAN/RAYLEIGH TECHNIQUE .....	6
3.0 DESCRIPTION OF EXPERIMENTAL FACILITY AND APPARATUS	
3.1 The Acoustic Research Tunnel (ART) .....	11
3.2 Initial Raman/Rayleigh Scattering Setup .....	12
3.3 Tunnel Calibration Raman/Rayleigh Scattering Setup .....	16
4.0 EXPERIMENTAL PROCEDURE	
4.1 Calibration .....	20
4.2 Data Acquisition .....	25
4.3 Data Reduction and Uncertainty .....	27
5.0 PRESENTATION AND DISCUSSION OF EXPERIMENTAL RESULTS	
5.1 Number Densities and Temperatures and Rayleigh Scattering Results from the Initial Experiments .....	38
5.2 Results from Tunnel Calibration Experiments .....	43
6.0 CONCLUSIONS AND RECOMMENDATIONS .....	47
REFERENCES .....	49

## ILLUSTRATIONS

### Figure

1. Spectrum of N <sub>2</sub> and O <sub>2</sub> in Air .....	7
2. N <sub>2</sub> and O <sub>2</sub> Rotational Raman Spectrum in Air .....	9
3. Acoustic Research Tunnel (ART) .....	11
4. Initial Raman/Rayleigh Experimental Arrangement in ART .....	13
5. Experimental Setup for Initial Raman/Rayleigh Measurements, South Side of ART .....	14
6. Experimental Setup for Initial Raman/Rayleigh Measurements, North Side of ART .....	15
7. Plan View of Tunnel Calibration Raman/Rayleigh Experimental Arrangement in ART .....	17
8. Experimental Setup for Tunnel Calibration Experiments, North Side of ART .....	18

<u>Figure</u>	<u>Page</u>
9. Experimental Setup for Tunnel Calibration Experiments, Bellmouth Inlet of ART .....	19
10. Rotational Raman Spectrum of N <sub>2</sub> and O <sub>2</sub> in Air .....	23
11. Calculated Values of R and C <sub>F2</sub> (T) as a Function of Rotational Temperature .....	24
12. Uncertainty in Free-Stream Mach Number .....	36
13. Uncertainty in Density Ratio as a Function of Mach Number .....	37
14. Density Boundary-Layer Profile, Mach Number 0.5, Flat Wall .....	39
15. Static Temperature Boundary-Layer Profile, Mach Number 0.5, Flat Wall .....	40
16. Free-Stream Density as a Function of Mach Number .....	41
17. Free-Stream Static Temperature as a Function of Mach Number .....	41
18. Free-Stream Density Obtained during Static Temperature Measurements as a Function of Mach Number .....	42
19. Free-Stream Static Temperature as a Function of Mach Number, Repeat .....	42
20. Free-Stream Density Obtained during Static Temperature Measurements as a Function of Mach Number, Repeat .....	43
21. Test Section Rayleigh Scattering Data as a Function of Mach Number, y = 2.5 in. ....	44
22. Ratio of Test Section and Stilling Chamber N <sub>2</sub> Number Densities versus Mach Number .....	45
23. Ratio of Test Section and Stilling Chamber N <sub>2</sub> Number Densities versus Mach Number, Repeat .....	45
24. Free-Stream Static Temperature as a Function of Mach Number, Tunnel Calibration Experiment .....	46
25. Free-Stream H <sub>2</sub> O Density as a Function of Mach Number .....	46
26. Ratio of Test Section H <sub>2</sub> O Density to Stilling Chamber N <sub>2</sub> Density as a Function of Mach Number .....	47

### TABLE

1. Uncertainties in Tunnel Parameters .....	37
NOMENCLATURE .....	50

## 1.0 INTRODUCTION

The development of sophisticated, high performance aerodynamic systems requires accurate flow-field measurements over a wide range of test conditions. In the past, these requirements were fulfilled by specially designed probes. However, a probe alters the flow field and complicates the problem of interpreting test results. Advances in electronics and laser technology have made it possible to perform measurements (which formerly required a probe) without disturbing the flow field. The nonintrusive laser techniques are particularly useful in performing measurements for which probes are not suited (e.g., hostile flow environments) and for situations where interference with the flow is not acceptable. Although the individual nonintrusive laser techniques do not provide the ultimate answer in flow-field measurements, each can provide important information. One such laser technique that has been under investigation and development at the Arnold Engineering Development Center (AEDC) is laser-Raman/Rayleigh scattering.

Laser-Raman/Rayleigh scattering has been used previously in the study of hypersonic flow fields (Refs. 1 and 2). These studies demonstrated the applicability of laser-Raman/Rayleigh scattering for hypersonic flow-field diagnostics. The attributes of the number density and temperature results are as follows: 1) no dependence on gas flow velocity, b) no dependence on gas molecule collision processes, c) "point" spatial resolution that decreases very little with increasing density and requires no inversion techniques common to absorption measurements and d) measurement precision which will increase with increasing gas density. It was the latter quality that made the prospect for successful subsonic flow-field measurements very promising because the hypersonic flow-field measurements had been conducted at gas number density levels of  $10^{16}$  to  $10^{17} \text{ cm}^{-3}$  and the subsonic flow number density level expected was  $10^{19} \text{ cm}^{-3}$ . Another attractive quality of laser-Raman scattering in particular is that the technique avoids the problem of particle lag suffered by the laser velocimeter in transonic flow with shock waves.

Recent observations in the AEDC Propulsion Wind Tunnel Facility (PWT) Aerodynamic Wind Tunnel (4T) and Propulsion Wind Tunnel (16T) have revealed measurement problems for which the Raman/Rayleigh scattering technique is well suited. There is evidence that wind tunnel calibration as well as measurements of lift coefficient and pitching moment are affected by humidity even if no visible condensation is present. Also, Ref. 3 suggests that wind tunnel calibration based on a correlation between centerline and plenum pressures may not be acceptable when a model with 1-percent blockage is installed. The ability of Raman/Rayleigh scattering to monitor the fluid properties nonintrusively makes it suitable for investigating these problems.



In this study two investigations were conducted to determine the applicability of performing Raman/Rayleigh scattering measurements in subsonic flow. The purpose of the initial investigation was to examine the problems associated with making Raman/Rayleigh scattering measurements of air number density, water vapor ( $H_2O$ ) number density, and static temperature in the subsonic-transonic flow regime. The second investigation was performed to apply the Raman/Rayleigh scattering technique to nonintrusive, online wind tunnel calibrations and humidity and condensation monitoring. Both investigations were conducted in the AEDC/PWT Acoustic Research Tunnel (ART).

## 2.0 THEORY OF RAMAN/RAYLEIGH TECHNIQUE

Detailed reviews of Raman/Rayleigh scattering can be found in Refs. 4 through 6; therefore, only a brief discussion need be undertaken here. Consider an intense, monochromatic laser beam consisting of photons of energy  $h\nu_0$  injected into a gas flow field. On collision with gas molecules, the photons may be elastically scattered, resulting in no change in the molecular internal energy states, and the scattered radiation is designated "Rayleigh scattering." Intensity of the scattered radiation for a particular detector location normalized to the incident laser beam intensity may be written as

$$I_{Ry} = C_{FRy} \sum_{i=1}^j n_i \sigma_i \quad (1)$$

in which  $n_i$  is the number density of the molecular species  $i$  with Rayleigh scattering cross section  $\sigma_i$ , and  $C_{FRy}$  is a constant that includes detection sensitivity. Since temperature variation in  $\sigma_i$  is justifiably neglected (Ref. 7), Eq. (1) can be rewritten as

$$I_{Ry} = C_{FRy} n \sum_{i=1}^j [X_i] \sigma_i \quad (2)$$

in which  $n$  is the total number density of the gas and  $[X_i]$  is the mole fraction of the  $i$ th species. It can be seen from Eq. (2) that for a gas mixture of constant mole fractions the Rayleigh scattered intensity is proportional to the total gas number density.

Inelastic collisions between laser photons and gas molecules cause a fraction of the molecules to undergo a quantum transition to a higher internal mode energy level with the result that the photon loses energy and is scattered with lower frequency (longer wavelength). The encounter with the photons can also cause the molecules to undergo transitions to a lower internal mode energy level, in which case the photon is scattered with increased frequency (shorter wavelength).

Figure 1 is a computer-generated Raman spectrum of nitrogen ( $N_2$ ) and oxygen ( $O_2$ ) in air showing the Rayleigh line and the Raman bands displaced to the long wavelength side (the Stokes side) only. The spectrum is a prediction of the spectrum that would be obtained with a Spex 0.5-m focal length double spectrometer with 1,200-groove/mm gratings, 750- $\mu$ m slits, and laser excitation at 5,145- $\text{\AA}$  wavelength. Located at approximately 5,846  $\text{\AA}$  is the Q-branch of the  $N_2$  vibration-rotation band. For a temperature range of 100 to 300 K and a relatively large spectral bandpass, the intensity of the band is essentially independent of temperature and directly proportional to the  $N_2$  number density,  $n(N_2)$ . That is,

$$I_m(N_2, Q) = C_F^{-1}(N_2) n(N_2) \quad (3)$$

in which  $I_m(N_2, Q)$  is the measured  $N_2$  band intensity normalized to the incident laser beam intensity and  $C_F(N_2)$  is a calibration factor. It can be seen from Eq. (3) that determination of  $C_F(N_2)$  and  $I_m(N_2, Q)$  will yield a measurement of  $n(N_2)$ .

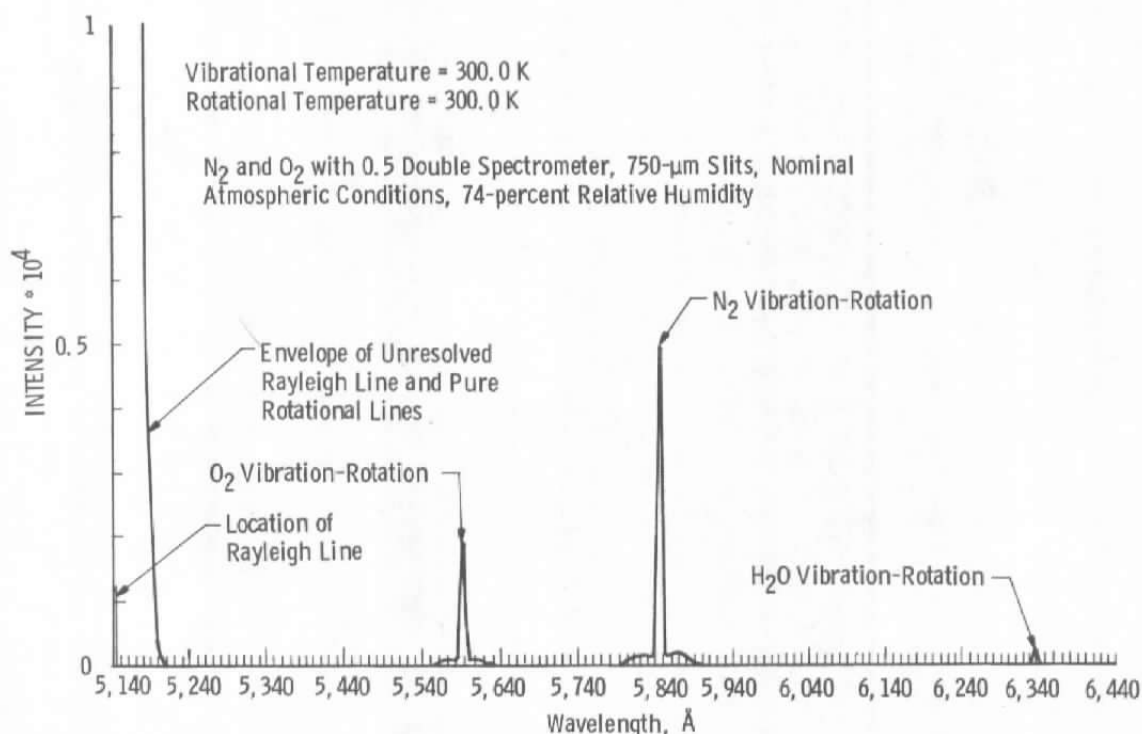


Figure 1. Spectrum of  $N_2$  and  $O_2$  in air.

Figure 2 is a computer-generated spectrum of the  $N_2$  and  $O_2$  rotational bands in air. The spectral bandpass has been narrowed (210- $\mu m$  slits) to give higher resolution than that used for Fig. 1. For the spectral resolution shown, the  $J = 6$  line of  $N_2$  and the  $J = 9$  line of  $O_2$  overlap at 5,160.9  $\text{\AA}$ , and the  $J = 12$  line of  $N_2$  and the  $J = 17$  line of  $O_2$  overlap at 5,173.7  $\text{\AA}$ . The intensity of a rotational line can be written (Ref. 1) as

$$I_m(J,X) = \frac{C_J n(X) e^{-J(J+1) \theta_X / T_R}}{q_R} \quad (4)$$

in which  $J$  is the rotational level quantum number,  $T_R$  is the rotational temperature,  $C_J$  is a quantum number-dependent parameter, and  $q_R$  is the rotational partition function. The quantity  $n(X)$  is the number density, and  $\theta_X$  is the characteristic rotational temperature of the species  $X$ . For example, for perfect spectral overlap the line intensity at 5,160.9  $\text{\AA}$  can be written as

$$I_m(J = 6,9; N_2 + O_2) = I_m(J = 6, N_2) + I_m(J = 9, O_2) \quad (5)$$

Of course the overlap is not perfect, but the Raman spectral program convolves the individual line intensities with the spectrometer instrument function and generates the peak line intensities

$$I_{c2} = I_c(J = 6,9; N_2 + O_2) \quad (6)$$

and

$$I_{c1} = I_c(J = 12,17; N_2 + O_2) \quad (7)$$

The calculated ratio of line intensities is a function only of temperature for a nonreacting, constant mole fraction gas mixture; i.e.,

$$\frac{I_{c1}}{I_{c2}} = R_c(T_R) \quad (8)$$

It is now possible to compare the measured value of the intensity ratio to a plot of  $R_c(T_R)$  as a function of  $T_R$  to determine a flow-field value of  $T_R$ . For the density regimes of the subsonic flow to be investigated  $T_R$  will be equal to the static temperature.

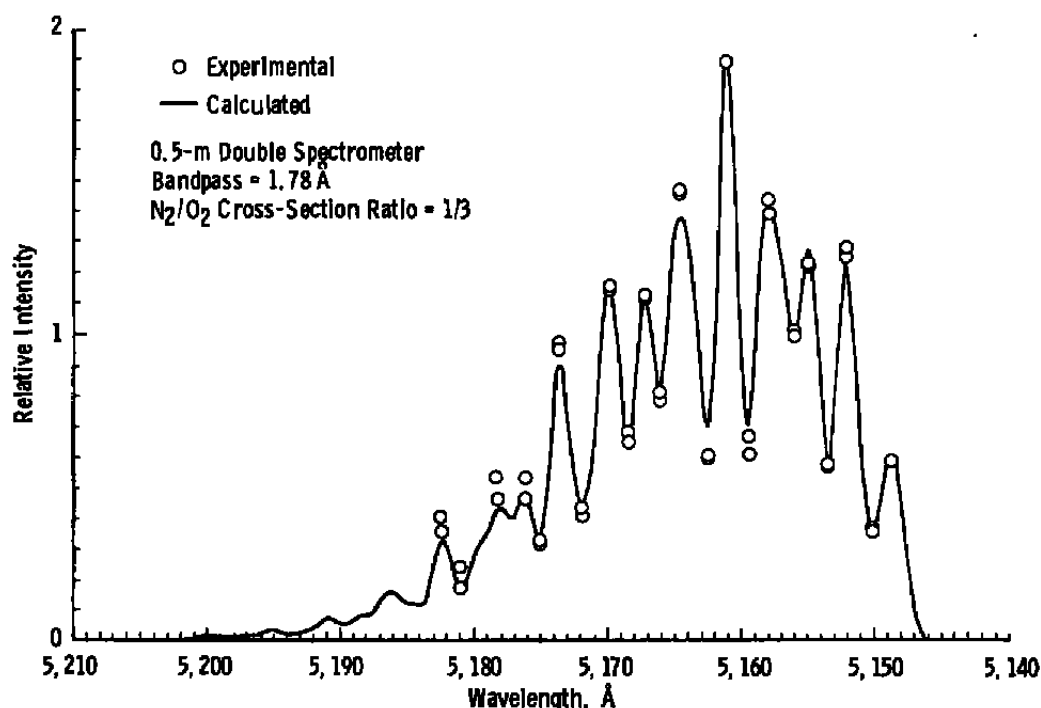


Figure 2.  $N_2$  and  $O_2$  rotational Raman spectrum in air.

Also shown in Fig. 1 is the main feature of the Raman vibrational spectrum of water vapor at moderate temperatures ( $< 600$  K). This spectral feature is the  $\nu_1$  band of  $H_2O$ , and it covers a spectral range of  $\approx 20$   $cm^{-1}$  at moderate temperatures. The  $\nu_1$  band shown in Fig. 1 is a trace of an experimental scan obtained in air at atmospheric pressure with a relative humidity of 74 percent. The experimental bandpass was the same as that used for the calculation of the  $N_2$  and  $O_2$  spectral features of Fig. 1. The  $\nu_1$  band origin has a Raman shift of about  $3,657.05$   $cm^{-1}$ , and for  $5,145$ - $\text{\AA}$  laser radiation this locates the band at  $\approx 6,337.4$   $\text{\AA}$ . According to Ref. 8 the ideal Raman displacement for measurement of  $H_2O$  number density is  $3,645.55$   $cm^{-1}$  or  $6,332.8$   $\text{\AA}$  for  $5,145$ - $\text{\AA}$  laser radiation, because the band centered about this position remains relatively constant with temperature variations for  $T \leq 600$  K. Therefore, for a comparatively large spectral bandpass centered at  $\approx 6,333$   $\text{\AA}$  the intensity will be essentially independent of temperature and directly proportional to the number density,  $n(H_2O)$ . That is,

$$I_m(H_2O, \nu_1) = C_F^{-1}(H_2O) n(H_2O) \quad (9)$$

and a calibration to determine  $C_F(H_2O)$  will permit measurement of  $n(H_2O)$ .

It is possible for a species such as  $H_2O$  to begin condensing in a subsonic flow field for certain regimes of the reservoir conditions and Mach number. Therefore, it can be important to detect this onset of condensation, and the Rayleigh scattering intensity can provide this information.

Equation (2) can be rewritten in the form

$$I_{Ry} = C_{FRy}^a n \sum_{i=1}^j [X_i] \alpha_i^2 \quad (10)$$

in which  $\alpha_i$  is the polarizability of the scatterer. The polarizability of each scatterer can be written classically in terms of its relative index of refraction,  $m$ , and its radius,  $a$ , as

$$\alpha = \frac{m^2 - 1}{m^2 + 2} a^3 \quad (11)$$

It has been assumed that the scatterer is spherical and that its ratio of radius to incident laser wavelength is

$$a/\lambda_0 \leq 0.05$$

For molecules and flow-field condensate these are reasonable assumptions. It can be seen from Eqs. (10) and (11) that as a species such as  $H_2O$  begins to condense and molecules begin to coalesce and grow in size the condensate contribution to  $I_{Ry}$  will increase with the sixth power of the cluster radius. It would therefore be expected that a sudden increase in  $I_{Ry}$  would indicate condensation onset; in fact, this has been observed for homogeneous nucleation in supersonic/hypersonic expansions (see Refs. 2 and 9).

Consideration of the polarization properties of both the incident and the Rayleigh scattered light reveals a second method for detection of condensation onset. For a linearly polarized laser beam and perfectly spherical scatterers, the polarization of the scattered light is parallel to that of the laser beam. For a gas mixture, such as air, the major constituents are diatomic or triatomic molecules, not spherical particles. Therefore, a small quantity of the Rayleigh scattered light exists with polarization components other than that parallel to the incident laser beam polarization. A Rayleigh scattering depolarization ratio can be defined as

$$\rho_L = \frac{I_{Ry}(\perp)}{I_{Ry}(\parallel)} \quad (12)$$

in which  $I_{Ry}(\perp)$  and  $I_{Ry}(\parallel)$  are the Rayleigh scattered intensities polarized perpendicular and parallel, respectively, to the polarization of the incident laser beam. It can be used to indicate condensation onset because as  $H_2O$  molecules condense and cluster together they form more spherical scattering centers which contribute more significantly to the scattered intensity. The depolarization ratio will therefore drop rapidly at condensation onset, and such drops have been observed for homogeneous nucleation in supersonic/hypersonic expansions (see Refs. 2 and 9).

### 3.0 DESCRIPTION OF EXPERIMENTAL FACILITY AND APPARATUS

#### 3.1 THE ACOUSTIC RESEARCH TUNNEL (ART)

The Acoustic Research Tunnel (ART) is an open-circuit, atmospheric indraft tunnel that is attached to the Plenum Evacuation System (PES) of the Tunnel 16T. The tunnel has a converging nozzle with a contraction ratio of 16, a 6-in.-square, 24-in.-long test section, and a 5-deg diffuser (see Fig. 3). The angle of the top and bottom walls in the test section can be varied from  $-0.5$  to  $+0.5$  deg, and a number of wall inserts are available to provide various wall porosities. Mach numbers from 0.05 to 1.10 can be generated in the ART when ventilated walls and test section wall divergence are used. Further details of the ART can be found in Ref. 10.

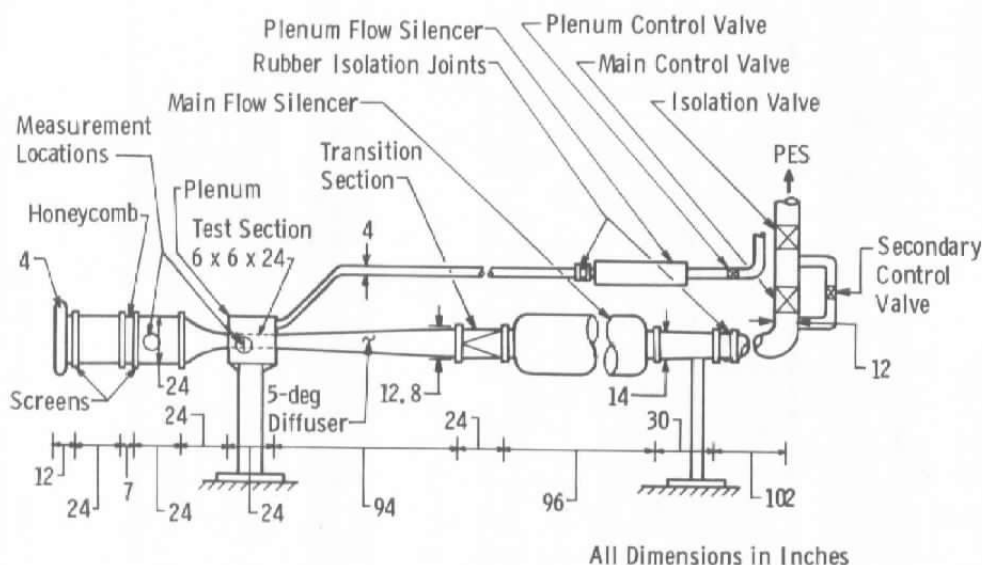


Figure 3. Acoustic Research Tunnel (ART).

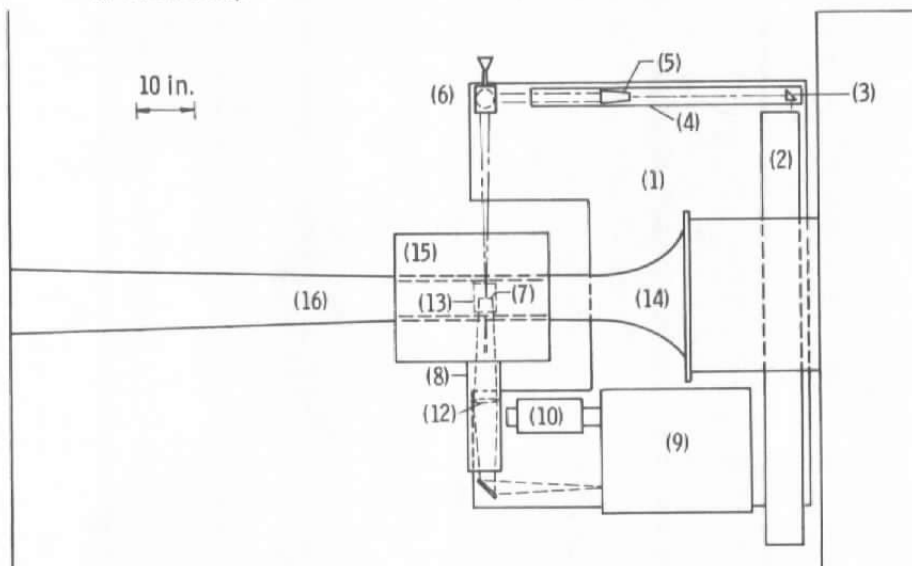
During both Raman/Rayleigh scattering investigations, impermeable walls and a constant area test section were used. This configuration limits the maximum Mach number to 0.85. For the initial investigation, the 8-in.-diam optical windows were replaced by inserts containing 3-in.-diam quartz windows to avoid possible damage to the regular windows caused by the high energy laser beam. Also, for the initial setup, optical windows were added to the bottom wall of the test section and plenum to provide a 90-deg viewing angle of the laser beam by the spectrometer (see Figs. 4a and b). For the tunnel calibration experiments the laser beam was directed down the tunnel centerline and viewed through 8-in.-diam windows located on the side wall of the stilling chamber downstream of the honeycomb and in the test section (see Fig. 3). Details of each Raman/Rayleigh experimental setup are presented in the following sections.

### 3.2 INITIAL RAMAN/RAYLEIGH SCATTERING SETUP

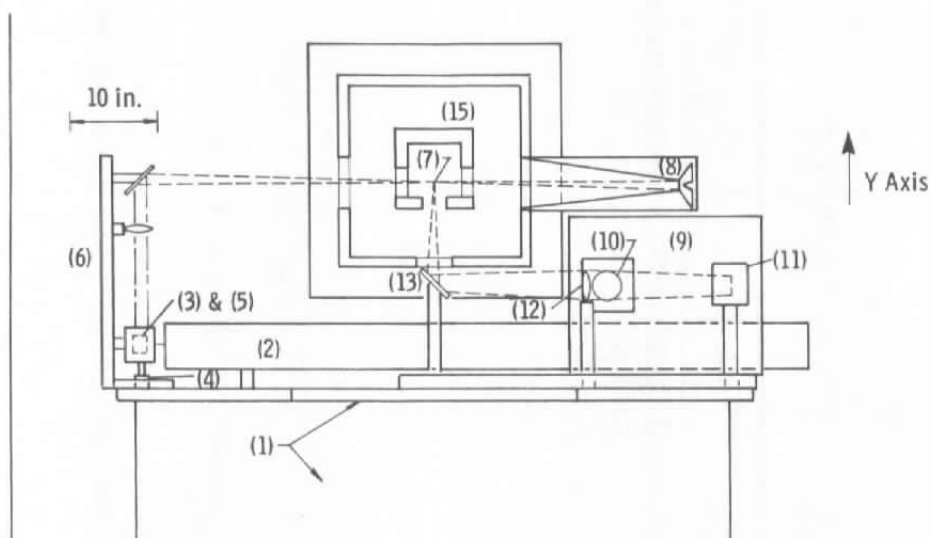
The initial Raman-Rayleigh experimental arrangement in the PWT-ART is shown schematically with two views in Figs. 4a and b as well as with photographs in Figs. 5 and 6. The entire optical system was mounted on a precision, three-dimensional traversing table located beneath the ART test section. A CR-18 argon-ion laser normally operated at 10 watts output at a wavelength of 5,145 Å was used as the excitation source for the Raman-Rayleigh scattering. The laser beam was expanded and focused onto the axial centerline perpendicular to the flow direction and parallel to the test section bottom wall. Following re-expansion, the beam entered a laser dump which prevented reflections from entering the test section. A 600-mm focal length collection lens was mounted underneath the test section to provide a collimated beam to an identical 600-mm focal length lens which imaged the laser beam focal volume onto the entrance slit of the 0.5-m focal length double spectrometer. A prism and several front surface mirrors were used for folding the light paths to permit mounting the complete optical system on the scan table. All transmission elements in the optical system were made of fused silica.

An aperture was located at the entrance slit of the spectrometer and adjusted so that a 0.25-in. length of the laser beam focal volume was observed by the spectrometer. Whenever a vibration-rotation band was observed, a high-pass filter was placed in front of the entrance slit to give additional rejection of the Rayleigh scattered light. A cooled (-26°C), RCA-C31034A photomultiplier tube (PMT) was mounted on the exit slit of the spectrometer for detection of the laser scattered light. A small quartz lens was used to image the radiation at the exit slit onto the photocathode of the PMT.

- |                                   |                                     |
|-----------------------------------|-------------------------------------|
| (1) Scan Table                    | (9) Spectrometer                    |
| (2) Ion Laser                     | (10) Photomultiplier Tube in        |
| (3) Prism                         | Thermoelectric Cooler               |
| (4) Optical Bar                   | (11) Mirror on Optical Bar          |
| (5) Beam Expander                 | (12) Collection Lens on Optical Bar |
| (6) Two Mirrors and Focusing Lens | (13) Mirror                         |
| on Vertical Optical Bar           | (14) Air Inlet                      |
| (7) Point of Measurement          | (15) Test Section                   |
| (8) Laser Dump                    | (16) Diffuser                       |



a. Plan view



b. End view

Figure 4. Initial Raman/Rayleigh experimental arrangement in ART.



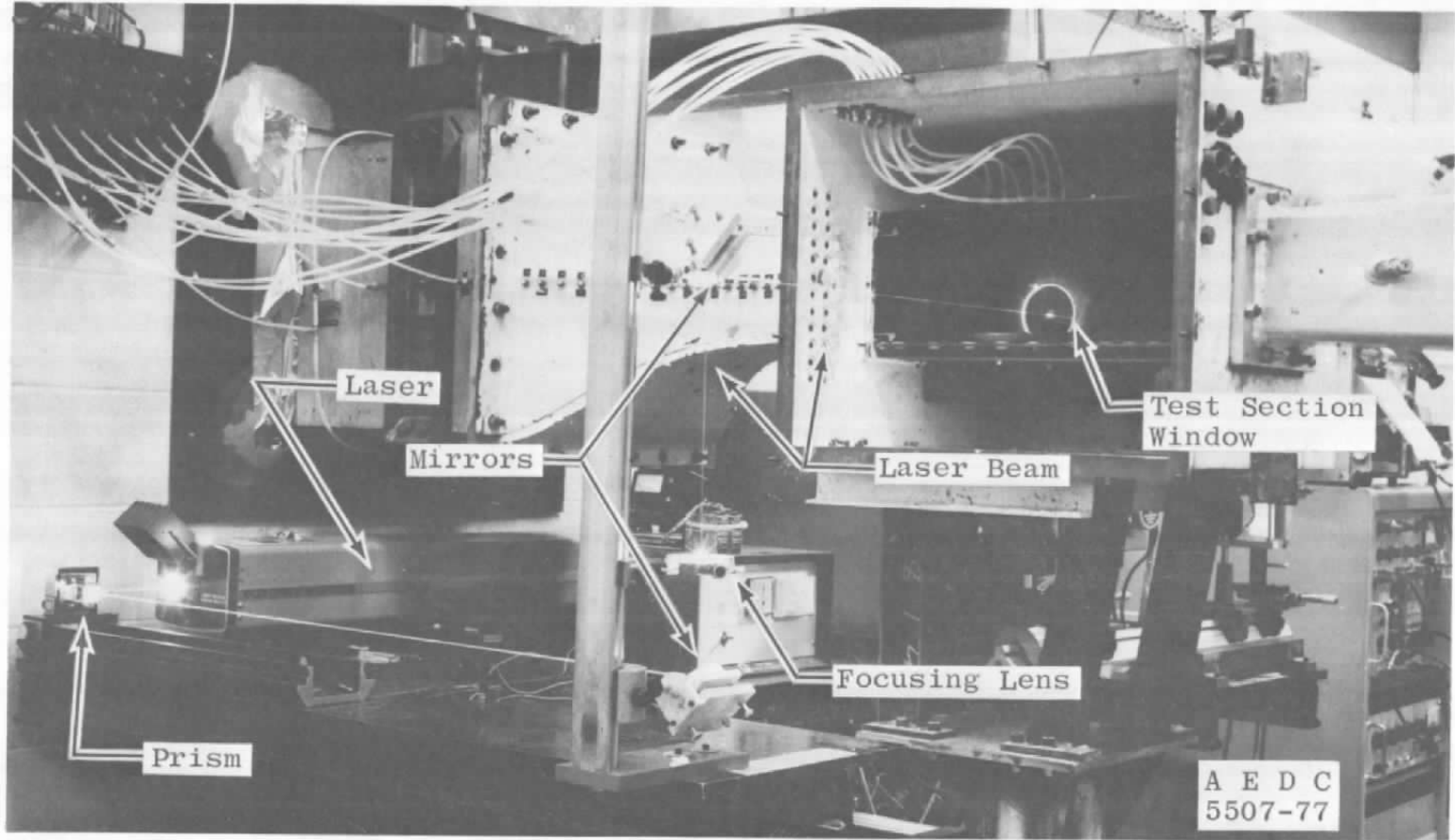


Figure 5. Experimental setup for initial Raman/Rayleigh measurements, south side of ART.

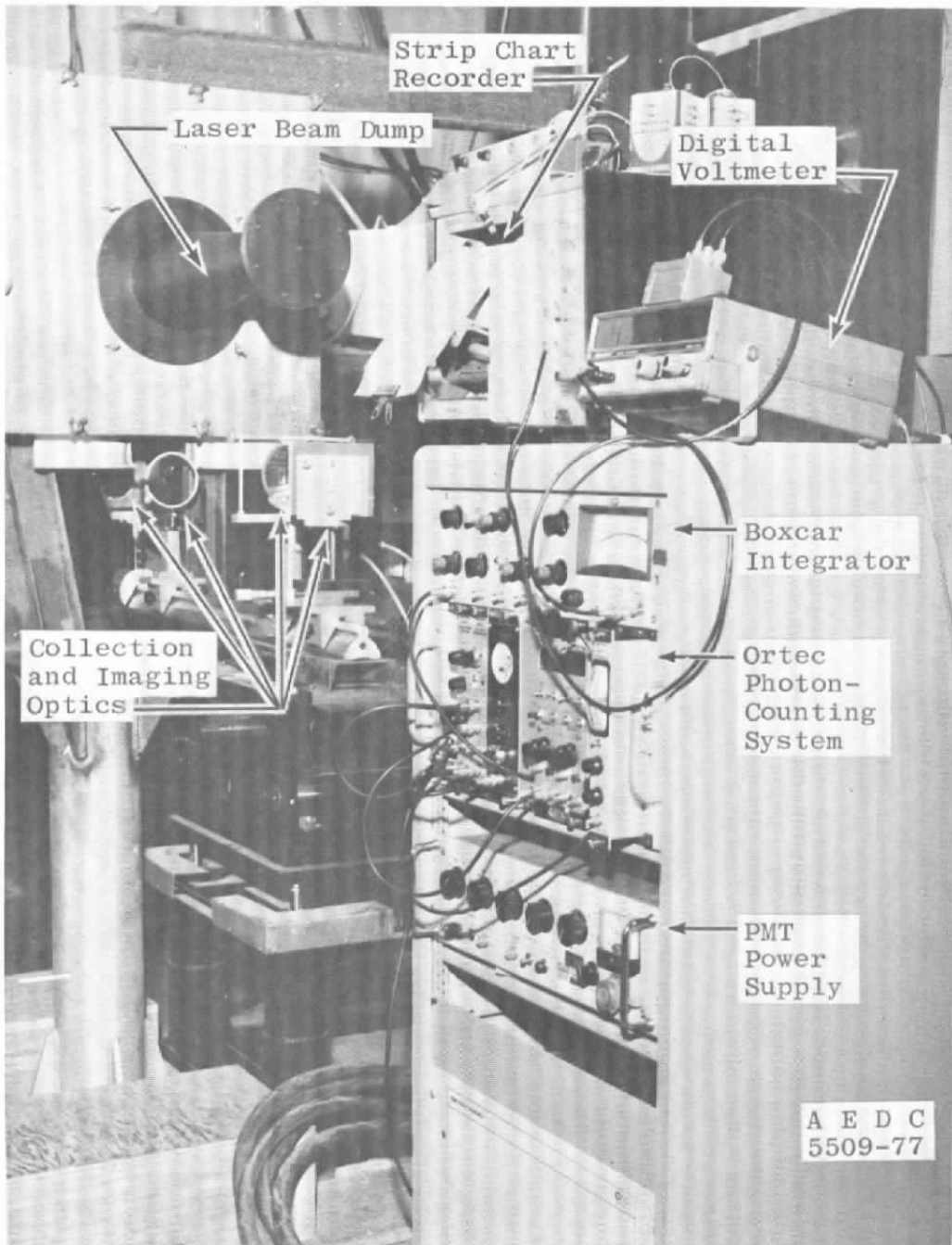


Figure 6. Experimental setup for initial Raman/Rayleigh measurements, north side of ART.

A Fluke 405B power supply provided 2,000 d-c volts to the PMT, and the output from the PMT was provided as a signal input to an Ortec Model 454 amplifier using a 50-ohm load resistor. The output from the amplifier was processed by an Ortec Model 436 discriminator, and the negative output of the discriminator was fed to an Ortec Model 715 counter/timer. The positive output of the discriminator was processed by an Ortec Model 449 ratemeter which provided an input to a strip chart recorder.

The output power of the laser was monitored by an internal photodiode assembly and displayed on an external meter. A modification to the assembly was made so that the photodiode output could be fed to a PAR boxcar integrator (Model CW-1). The output of the integrator was displayed by a digital voltmeter. Integrating the value of the laser power over a measurement interval allowed a measure of the laser energy used during the measurement interval to be obtained.

Figure 5 (photograph) shows the laser beam (with beam expander removed) deflected and focused onto the test section axial centerline. The plenum and test section walls on the beam input side were removed for this photograph. Figure 6 is a view of the laser beam dump, collection and imaging optics, Ortec photon-counting system, boxcar integrator, digital voltmeter, strip chart recorder, and PMT power supply.

### 3.3 TUNNEL CALIBRATION RAMAN/RAYLEIGH SCATTERING SETUP

The tunnel calibration experimental arrangement is shown schematically in Fig. 7 and photographically in Figs. 8 and 9. A major portion of the optical system was again mounted on the precision scan table; however, the scan table was not used for scanning in the tunnel calibration experiments. The CR-18 argon-ion laser was oriented on the scan table as shown in Figs. 7 and 8 so that the beam passed through an opening in the wall separating the test section room from the ART air intake room. Reflective prisms oriented the laser beam so that it passed through the bellmouth inlet (see Fig. 9) and along the axial centerline of the tunnel and through the test cell, finally impinging on an acoustic filter in the output ducting. A half-wave plate was used at the laser output to rotate the vertically polarized beam to horizontal polarization, thereby providing a vertically polarized beam in the tunnel.

Scattered light was collected from the test section with a 6-in. focal length lens set up to give a 1:1 image at the entrance slit of a 0.85-m focal length double spectrometer. A dove prism was placed at the entrance slit of the spectrometer to orient the image of the laser beam path along the vertical spectrometer slit. An aperture at the entrance slit defined a 0.25-in. beam length for observation. Whenever rotational Raman scattering was observed, a polarization scrambler plate was also placed in front of the entrance slit. As shown in Figs. 7 and 8 the laser dump used in the initial Raman-Rayleigh setup was used as a viewing dump

for the test section collection optics. Radiation from the spectrometer exit slit was again focused by a coupling lens onto the photocathode of an RCA-C31034A PMT cooled to  $-26^{\circ}\text{C}$ .

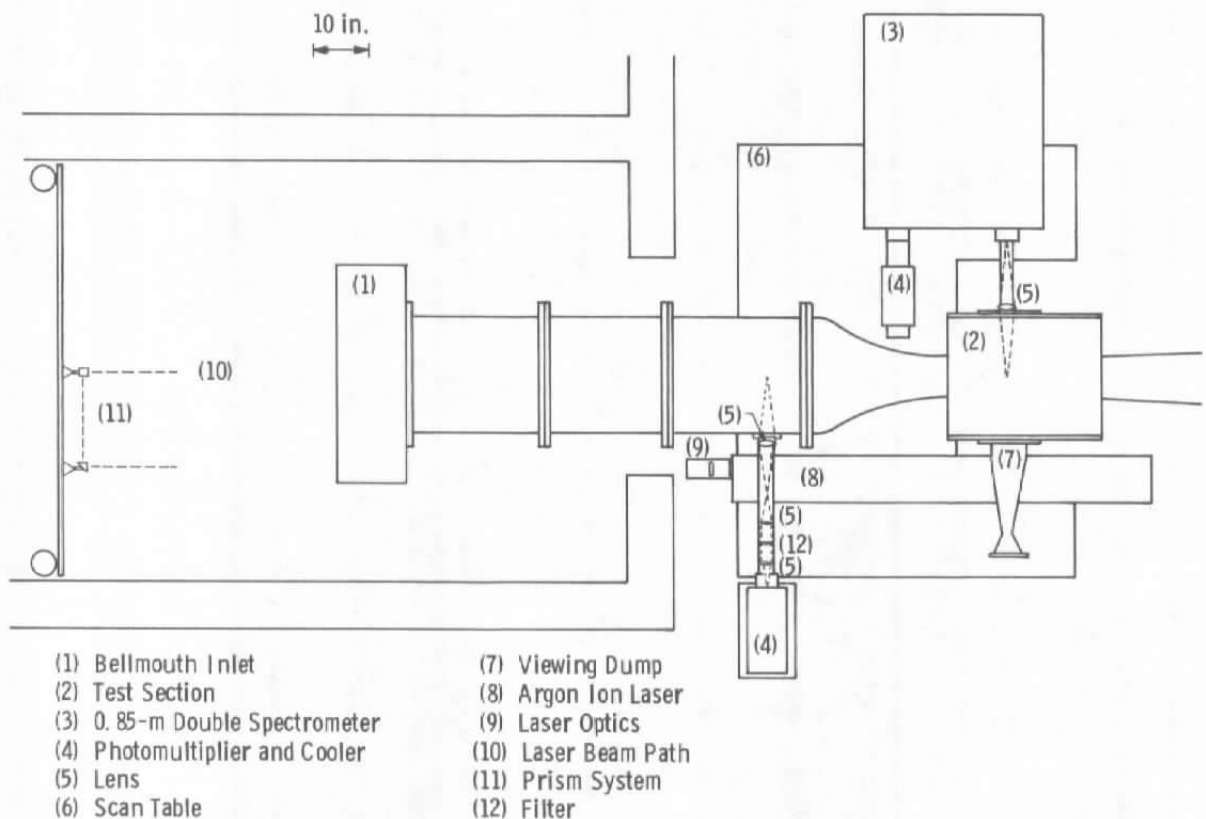


Figure 7. Plan view of tunnel calibration Raman/Rayleigh experimental arrangement in ART.

Scattered light was collected from the stilling chamber with a 150-mm focal length lens and imaged upon an adjustable iris aperture that was set for observation of a 0.25-in. beam length. Radiation transmitted through the aperture was collimated with a 63-mm focal length lens and imaged with a 150-mm focal length lens onto the photocathode of a cooled ( $-26^{\circ}\text{C}$ ) RCA-C31034A PMT. The collimated beam path was used for placement of interference filters and a high-pass filter for rejection of Rayleigh scattered light.

Power to both photomultipliers was provided by a Fluke 408B power supply operating at -2,000 volts. Outputs from the photomultipliers were measured across 50-ohm loads and processed by Ortec photon-counting equipment. Each PMT signal was fed through a Model

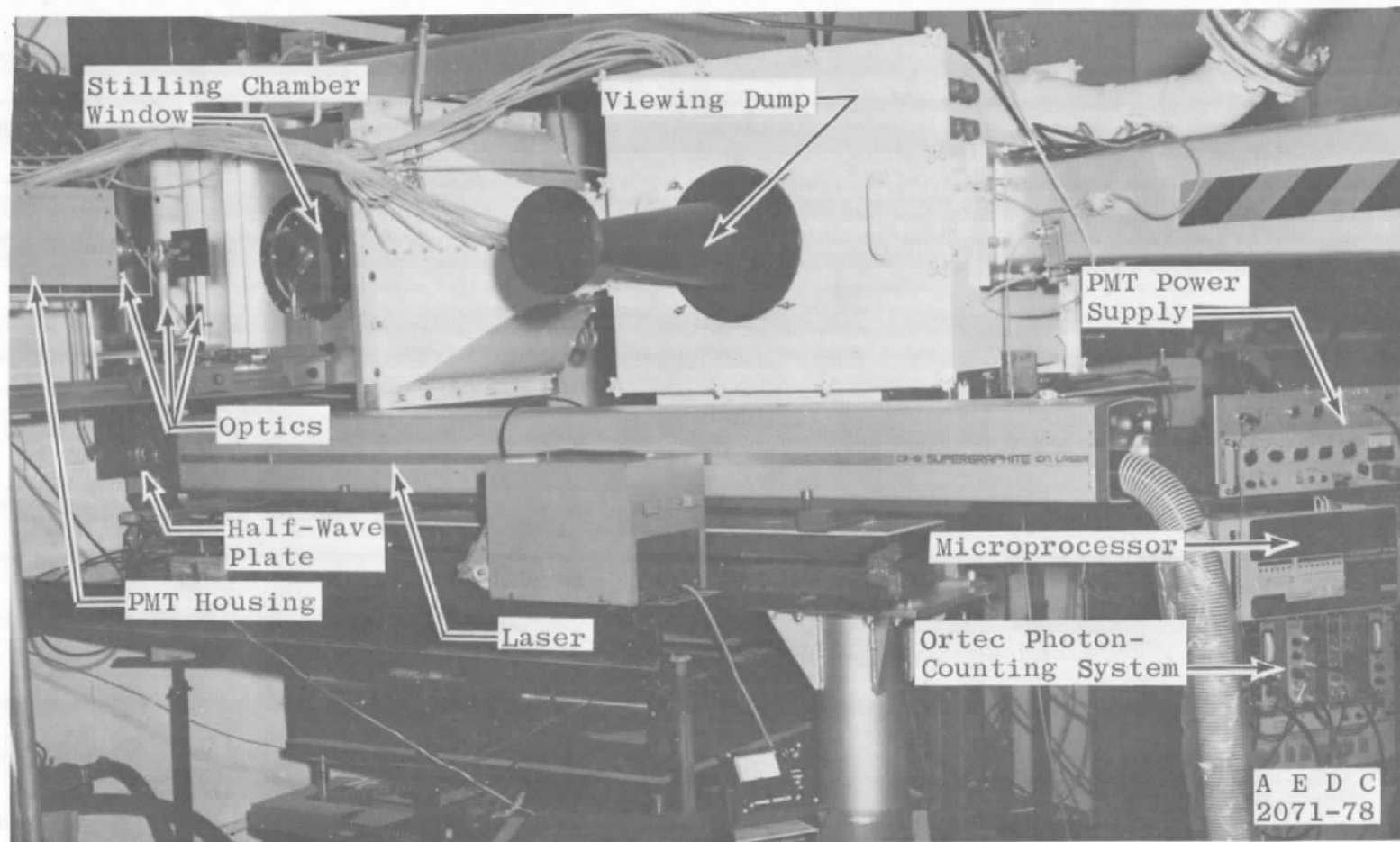


Figure 8. Experimental setup for tunnel calibration experiments, north side of ART.

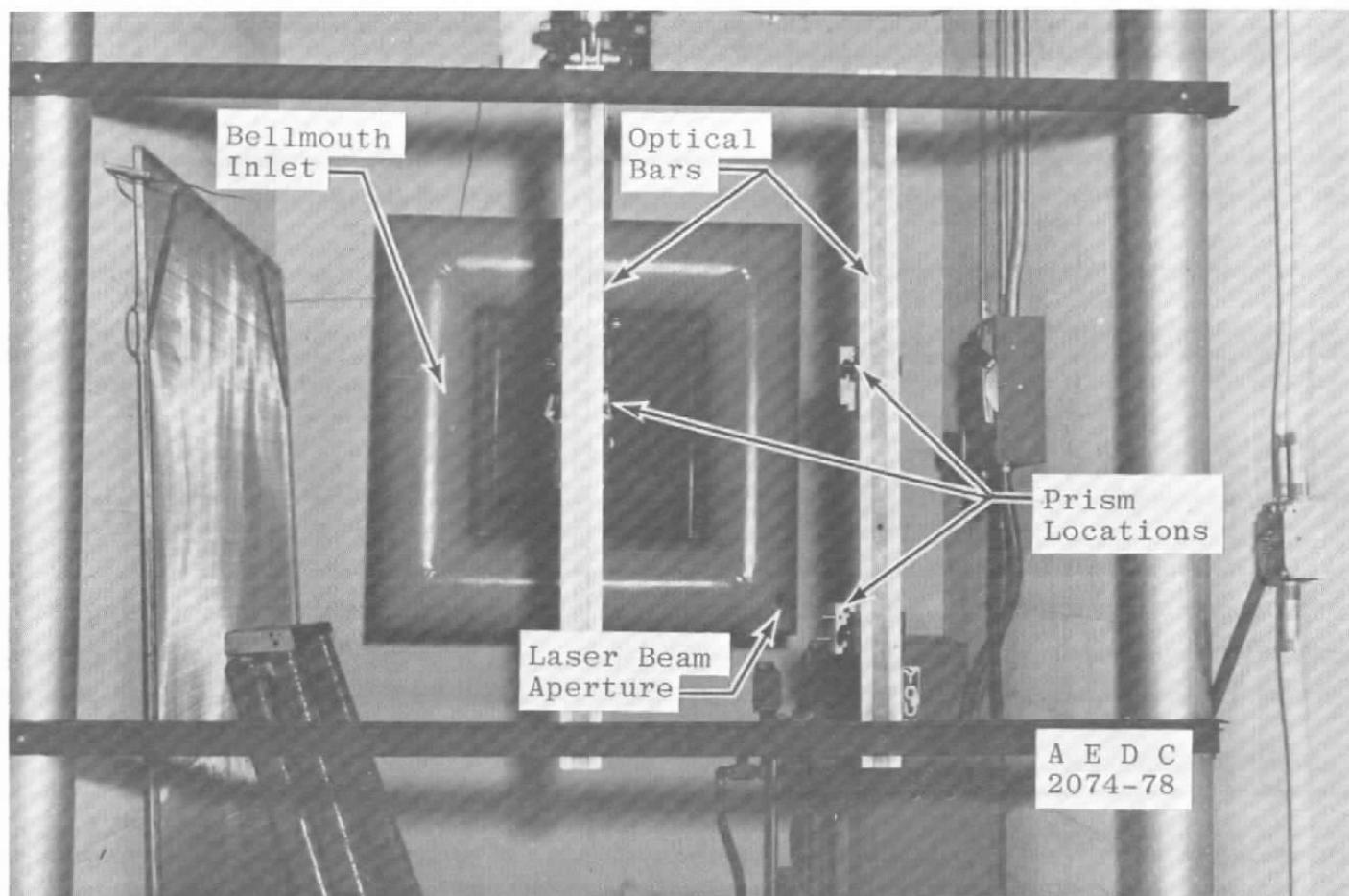


Figure 9. Experimental setup for tunnel calibration experiments, bellmouth inlet of ART.

454 amplifier, a Model 436 discriminator, and a Model 772 counter. Timing was controlled by a Model 773 counter/timer. Positive signals from each of the discriminators were also fed to Model 441 ratemeters for subsequent strip chart display. Data acquisition as well as spectrometer wavenumber setting was controlled by a microprocessor system with output to a teletype.

#### **4.0 EXPERIMENTAL PROCEDURE**

The experimental procedure for both Raman/Rayleigh scattering experiments can be summarized as outlined below.

1. Pre-test calibrations were performed on the tunnel flow-monitoring equipment and the Raman/Rayleigh scattering instrumentation.
2. The desired flow conditions were established at a reference position at the same axial location as the laser probe volume in the test section. Each flow condition was established either by varying Mach number at a fixed measurement location or by varying measurement location at a fixed Mach number. Both modes of operation were used in the initial experiments, but only the first was used in the tunnel calibration experiments.
3. Raman/Rayleigh scattering data and tunnel flow conditions were recorded at each Mach number or measurement location.

Detailed procedures regarding calibration, data acquisition and data reduction are presented in the following sections.

#### **4.1 CALIBRATION**

##### **4.1.1 Raman/Rayleigh Scattering Equipment**

Before beginning calibrations the PMT's were cooled for approximately 24 hours and exposed to the low-level Raman signals for approximately 1 hour. The calibration of the Raman/Rayleigh scattering was completed prior to an ART test period. The test section was opened to the bellmouth inlet, and the outside doors of the air inlet room were opened. Atmospheric pressure values were provided by AEDC Power Control personnel. During calibrations for the initial experiments relative humidity values were determined from wet and dry bulb values supplied by AEDC Power Control. During tunnel calibration experiments the wet and dry bulb values were determined directly in the air inlet room. Test

section temperatures and standard relative humidity tables were used to determine relative humidity and H<sub>2</sub>O saturation vapor pressure. The wet air number density was determined as follows:

$$n_w^o(\text{air}) = \frac{P^o(\text{air}) 0.966 \times 10^{19}}{T^o} \quad (13)$$

The water vapor number density was determined from

$$n^o(\text{H}_2\text{O}) = \frac{\text{RH}}{100} \left[ \frac{P_s^o(\text{H}_2\text{O}) 0.966 \times 10^{19}}{T^o} \right] \quad (14)$$

Therefore, the dry air number density was

$$n_d^o(\text{air}) = n_w^o(\text{air}) - n^o(\text{H}_2\text{O}) \quad (15)$$

Since the ratio of N<sub>2</sub> to O<sub>2</sub> number density remained constant in the ART flowfield, the N<sub>2</sub> vibration-rotation band at 5,846 Å was used for measurements of dry air number density. The band was monitored for a sufficiently long interval,  $\tau_s$  (nominally 100 sec), during which photon counts ( $N_s$ ) were accumulated and the laser power was integrated to give a laser energy value,  $E_o(\tau_s)$ . The laser beam path was subsequently blocked, and background photon counts were accumulated over an arbitrarily long interval,  $\tau_B$  (nominally 50 sec). The contribution of the background to the signal level was determined from

$$N_B(\tau_s) = N_B(\tau_B) \left( \frac{\tau_s}{\tau_B} \right) \quad (16)$$

The Raman signal was determined from

$$N_m(N_2, Q) = N_s(\tau_s) - N_B(\tau_s) \quad (17)$$

and the energy-normalized intensity was

$$I_m^o(N_2, Q) = N_m(N_2, Q) / E_o(\tau_s) \quad (18)$$

in which

$$E_o(\tau_s) = \int_0^{\tau_s} P_o dt \quad (19)$$



where  $P_0$  is the laser output power.

A calibration factor for conversion of energy-normalized Raman intensity to dry air number density was calculated from

$$C_F(\text{air}) = n_d^0(\text{air}) / I_m^0(N_2, Q) \quad (20)$$

For those test periods during which radial surveys of the flow field were to be made, an additional calibration had to be performed to determine the variation of  $C_F(\text{air})$  with radial (vertical) position of the laser beam focal volume within the flow. This calibration was necessary because of beam transmission differences through different parts of the entrance ports and because of collection optics transmission variations as a result of the changing area of the viewing port used by the collection lens. A transmission factor was determined from

$$T_F(y) = \frac{I_m^0(N_2, Q, y)}{I_m^0(N_2, Q, y = 2.5)} \quad (21)$$

Calibration for temperature measurements primarily involved a comparison of experimental rotational spectra with calculated spectra generated by the Raman spectral program. A typical spectrum obtained in air with the 0.5-m spectrometer is shown in Fig. 10. By varying spectral bandpass values and the relative value of  $N_2$  and  $O_2$  rotational Raman cross sections a close approximation to the experimental spectra could be calculated. Figure 2 shows the predicted spectrum calculated using a bandpass of 1.78 Å and an  $O_2$ -to- $N_2$  cross-section ratio of three. Experimental peak and valley intensities normalized to the largest peak value of the predicted spectrum are also shown. The predicted intensity ratio was always within 10 percent of the measured ratio without a polarization scrambler, and it was within 5 per cent when a polarization scrambler was used. Figure 11 shows a plot of the predicted intensity ratio,  $R_c(T_R)$ , as a function of air rotational temperature. For the temperature range of interest the curve is linear; therefore, a correction factor can be used to account for the difference between measured and predicted intensity ratios for the atmospheric, nominally room temperature calibration conditions. The correction factor is

$$C_F(T) = R_c^0 / R_m^0 \quad (22)$$

in which  $R_m^0$  is the measured value of the intensity ratio.

Whenever temperature measurements were made, a simultaneous determination of density was possible, because both  $I_{m1}$  and  $I_{m2}$  are directly proportional to the dry air

number density [see Eq. (4)]. Because of its higher relative intensity,  $I_{m2}$  was always chosen for density determination. The calibration factor for conversion of the  $I_{m2}$  value to dry air number density was calculated from

$$C_{F2} = n_d^0(\text{air}) / I_{m2}^0 \quad (23)$$

Of course the variation of  $I_{m2}$  with temperature had to be taken into consideration whenever an air number density was determined. A temperature-dependent correction factor was calculated from

$$C_{F2}(T) = I_{c2}^0 / I_{c2}^T \quad (24)$$

and the variation of  $C_{F2}(T)$  with temperature is shown in Fig. 11.

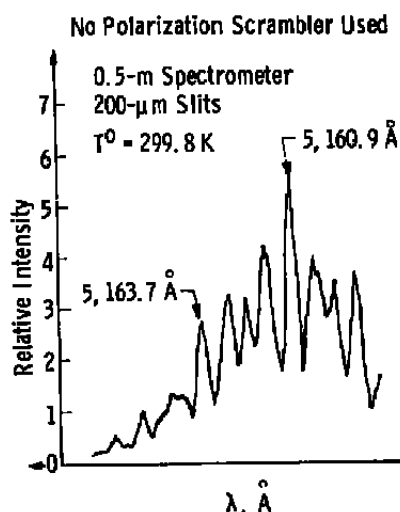


Figure 10. Rotational Raman spectrum of  $N_2$  and  $O_2$  in air.

A calibration factor for determination of  $H_2O$  number density was calculated from

$$C_{F1}(H_2O) = n^0(H_2O) / I_m^0(H_2O, \nu_1) \quad (25)$$

It was assumed that over the small range of temperature variation for the ART test conditions  $I_m(H_2O, \nu_1)$  was independent of temperature. This was a valid assumption because of the proper selection of the spectrometer setting and the wide spectral bandpass ( $\approx 9.1 \text{ Å}$ ) used.

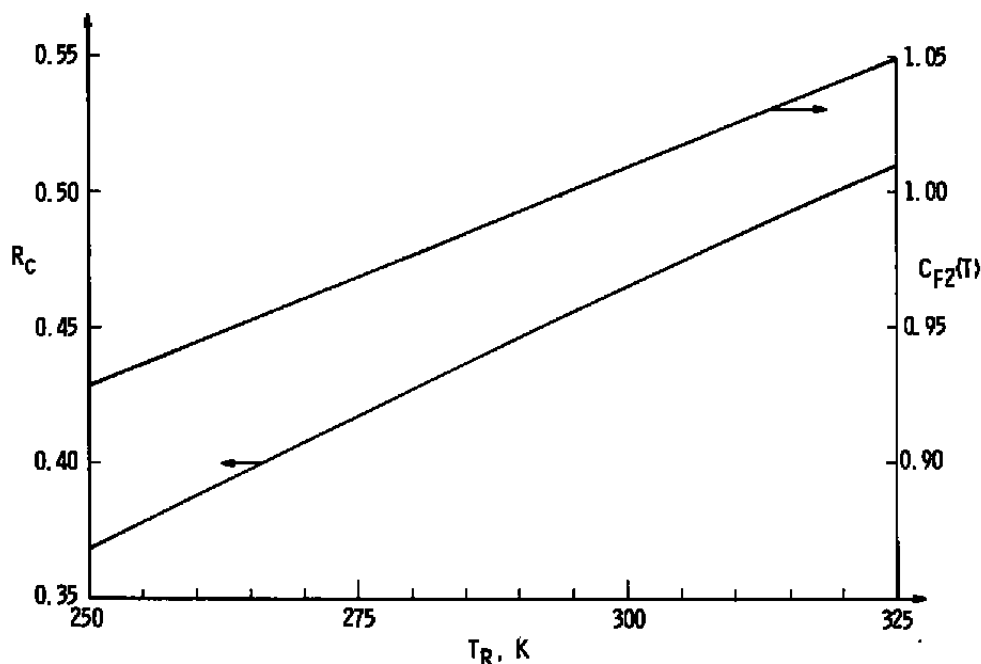


Figure 11. Calculated values of  $R$  and  $C_{F2}(T)$  as a function of rotational temperature.

Because the test section could not be evacuated to a sufficiently low pressure, no attempt was made to determine calibration factors for the Rayleigh scattering intensity or depolarization ratio. That is, without evacuation of the test section the contribution to the Rayleigh scattering intensity from laser beam light reflecting from test section walls could not be evaluated. It was assumed that the fraction of light reflected from the walls would remain constant, and it was further assumed that flow-field Rayleigh scattering reflected from the walls and into the spectrometer was minimal.

#### 4.1.2 Tunnel-Monitoring Equipment

Flow conditions in the ART were calculated from measurements of total and static pressures and total and static temperatures. During the Raman/Rayleigh scattering experiments, additional measurements of wet and dry bulb temperatures were required to determine humidity levels in the air.

The tunnel pressures were monitored by the pressure scanning system. The system used a Kistler® series 314 0- to 15-psi pressure transducer to convert tunnel pressures to a d-c voltage signal. The output of the transducer was displayed on a digital voltmeter. Prior to each run, the pressure transducer was calibrated over the range from 0 to 2,000 psf. The zero

point was established by venting both sides of the transducer to atmosphere, and the span was set by application of a known pressure to the transducer while the reference side was exposed to a vacuum. Several known pressures were applied to check the linearity of the transducer over the calibration range. The signal from the transducer was conditioned so that the pressure could be read directly in psf on the digital voltmeter.

Copper-constantan thermocouples were used to measure tunnel total and static temperatures. The thermocouple system was calibrated prior to the Raman/Rayleigh experiments using secondary standards whose uncertainties are traceable to the National Bureau of Standards calibration equipment.

Relative humidity was determined by measurements of wet and dry bulb temperature using a psychrometer with mercury thermometers. The instrument was calibrated against secondary standards as recommended by the National Bureau of Standards.

## 4.2 DATA ACQUISITION

During the initial Raman-Rayleigh scattering experiments several distinct types of data were acquired, as follows:

- a.  $n(\text{air})$  as a function of Mach number at  $y = 2.5$  in. from the bottom wall of the test section
- b.  $T_R$  and  $n(\text{air})$  as a function of Mach number at  $y = 2.5$  in. from the bottom wall of the test section
- c.  $I_{Ry}$  and  $q_L$  as a function of Mach number at  $y = 2.5$  in. from the bottom wall of the test section
- d.  $n(\text{air})$  as a function of vertical distance ( $y$ ) from the bottom wall of the test section
- e.  $T_R$  as a function of vertical distance ( $y$ ) from the bottom wall of the test section

For each type of data the acquisition procedure was generally the same. Before each data point was taken the collection optics and laser power were adjusted for maximum photon count rate at the selected spectrometer wavelength setting. When tunnel conditions and/or the scan table vertical position were properly set, the photon counting instrumentation was reset, and photon counts were accumulated until a level of at least  $\approx 200K$  counts was reached. Accumulated counts, counting duration in seconds, and the time-integrated power

displayed in volts by a DVM were recorded by hand. The laser beam was then blocked off at the laser head, and background counts were accumulated for a duration approximately twice as long as that used for signal measurements. Counts and time were again recorded by hand. For measurements of  $T_R$  or  $q_L$  this procedure had to be followed twice for each data point. Furthermore, for  $T_R$  measurements a wavelength change had to be made for each data point, and for  $q_L$  measurements 90-deg rotation of a Polaroid® sheet, which was mounted at the spectrometer entrance, had to be effected for each data point. For simultaneous  $T_R$  and  $n(\text{air})$  measurements the spectrometer slits were 200  $\mu\text{m}$  wide. The slit widths were set at 2 mm for  $n(\text{air})$  measurements using the  $\text{N}_2$  vibration-rotation band, and for Rayleigh scattering measurements the slits were narrowed to 100- $\mu\text{m}$  width.

Data acquisition for the tunnel calibration experiments was somewhat different. The types of data acquired are listed as follows:

- f. ratio of test section axial centerline air number density to stilling chamber air number density,  $n(\text{air})/n_0$ , as a function of Mach number
- g. ratio of test section axial centerline  $\text{H}_2\text{O}$  number density to stilling chamber air number density,  $n(\text{H}_2\text{O})/n_0$ , as a function of Mach number
- h.  $T_R$  on the test section axial centerline as a function of Mach number.

For these data types the acquisition was accomplished with a microprocessor system (MPS), and commands to the MPS were entered via a teletype. Before each data point the collection optics and laser power were adjusted for maximum photon count rate. When tunnel conditions were properly set, the photon-counting instrumentation was reset, and photon counts were accumulated until at least 200K counts were reached with each data channel for data types f and h. For data type g, only 10K counts were accumulated on the spectrometer channel because of the low signal level of the  $\text{H}_2\text{O}$  band. Accumulated counts, counting duration, and time-integrated power were recorded by the MPS and output via the teletype upon command. It should be noted that although the filter channel sensitivity was nearly an order of magnitude higher than that of the spectrometer channel the count rates of each channel were approximately equalized with different discriminator settings when types f and h data were obtained. The laser beam was then blocked off at the laser head, and background counts were accumulated for a duration equal to that used for the signal measurements. Wavelength settings for the temperature measurements were controlled by the MPS. Spectrometer slits for  $n(\text{air})$  and  $n(\text{H}_2\text{O})$  measurements were 3 mm wide (9.1-Å bandpass), and for  $T_R$  measurements they were narrowed to 500  $\mu\text{m}$  wide (1.5-Å bandpass). The interference filter used in the filter channel for monitoring the  $\text{N}_2$  vibration-rotation band was centered at 5,843 Å and had a 23-Å bandpass.

At each Raman/Rayleigh test condition, tunnel pressures and temperatures were hand recorded. Relative humidity during a test period remained essentially constant; therefore, wet and dry bulb temperatures were recorded at regular time intervals instead of at each test condition. During the initial experiments the wet and dry bulb temperatures were supplied by AEDC Power Control, and during the tunnel calibration experiments the values were measured in the ART inlet room. Comparison of the values from both sources indicated excellent agreement.

### 4.3 DATA REDUCTION AND UNCERTAINTY

#### 4.3.1 Raman/Rayleigh Data

Air number density values were determined primarily using the relation

$$n(\text{air}) = C_F(\text{air}) I_m^t(N_2, Q) / T_F(y) \quad (26)$$

H<sub>2</sub>O number density values were determined using the relation

$$n(\text{H}_2\text{O}) = C_F(\text{H}_2\text{O}) I_m^t(\text{H}_2\text{O}, \nu_1) \quad (27)$$

Rotational (static) temperature values were determined by calculating

$$R_m^t = C_F(T) I_{m1}^t / I_{m2}^t \quad (28)$$

and graphically reading a value of temperature from a plot of  $R_c$  as a function of temperature.

Air number density values determined during the temperature measurement process were found by using the relation

$$n(\text{air}) = C_{F2} C_{F2}(T) I_{m2}^t \quad (29)$$

Evaluation of the total uncertainty,  $U$ , of the Raman/Rayleigh measurements was made using the relation

$$U = \pm(B + S) \quad (30)$$

in which  $B$  is the size of the credible bound to the systematic error and  $S$  is the confidence limit on the random or standard deviation. For determination of the random error the photon-counting error relations of Ref. 11 were used. For a background-corrected spectral signal,  $N_m$ , the fractional standard deviation is

$$\sigma(N_m) = \frac{\sqrt{N_s + N_B} \eta^2}{N_s - N_B \eta} \quad (31)$$

in which  $N_s$  and  $N_B$  are the signal counts and background counts accumulated, respectively, and  $\eta$  is the ratio of time duration for measurement of  $N_s$  to time duration for measurement of  $N_B$ ; that is,

$$\eta = \tau_s / \tau_B \quad (32)$$

Measuring  $n(\text{air})$  and  $T_R$  during the initial experiments yielded background count rates typically two orders of magnitude less than the signal rate, and  $\eta$  was typically 1/2. Evaluation of Eq. (31) then yields

$$\sigma(N_m) \approx 0.002 \quad (33)$$

During the initial experiments the random error of the laser power integrator was measured to be

$$\sigma(E_o) = 0.007 \quad (34)$$

Therefore, the random error for a Raman intensity measurement during the initial experiments was

$$S^{(1)}(I_m, \text{air}) = \sqrt{[\sigma(N_m)]^2 + [\sigma(E_o)]^2} \approx 0.0073 \quad (35)$$

Because a temperature measurement involves determination of an intensity ratio, the random error for an intensity ratio was

$$S^{(1)}(R) = \sqrt{[S^{(1)}(I_{m1})]^2 + [S^{(1)}(I_{m2})]^2} \approx 0.0103 \quad (36)$$

For the Rayleigh scattering measurements the background count rate was negligible. Counts accumulated were approximately 400K for  $I_{Ry}(\parallel)$  and 200K for  $I_{Ry}(\perp)$ . Equations (31), (32), and (35) gave random error for the Rayleigh intensity measurements as

$$S[I(1)] \approx S[I(L)] \approx 0.007 \quad (37)$$

and for the depolarization ratio

$$S(\rho_L) \approx 0.0099 \quad (38)$$

Evaluation of systematic error for the initial experiments requires determination of the total uncertainty in the measurement of the calibration factors. The accuracy of the atmospheric pressure and test section temperature values was estimated at  $\pm 1$  percent and  $\pm 1.5$  percent, respectively. Therefore the systematic error for determination of  $C_F(\text{air})$  was calculated to be

$$B[C_F(\text{air})] = \sqrt{(0.01)^2 + (0.015)^2 + (0.0073)^2} \approx 0.0194 \quad (39)$$

The total uncertainty for  $n(\text{air})$  was

$$U^{(1)}[n(\text{air})] = 0.0267 \quad (40)$$

for measurements using the Q-branch of the  $N_2$  vibration-rotation band. Because of the additional correction factor needed when density boundary-layer profiles were made, the total uncertainty for  $n(\text{air})$  in the boundary-layer profile was

$$U^{(1)}[n(\text{air})] = 0.0293 \quad (41)$$

The systematic error for determination of the correction factor  $C_F(T)$  used for temperature measurements was

$$B^{(1)}[C_F(T)] = 0.0103 \quad (42)$$

Therefore, the total uncertainty for the measured intensity ratio  $R_m$  was calculated to be

$$U^{(1)}(R) = 0.0206 \quad (43)$$

The total uncertainty in temperature,  $T_R$ , was determined by developing the relation

$$\Delta T \approx \Delta R \frac{dT}{dR} \quad (44)$$



$$\Delta T \equiv U(T_R) T_R \quad (45)$$

$$\Delta R \equiv U(R) R \quad (46)$$

Therefore

$$U(T_R) \approx \frac{U(R) R}{T_R \left( \frac{dR}{dT} \right)_{T_R}} \quad (47)$$

Evaluating Eq. (47) at  $T_R = 295 \text{ K}$  gives

$$U^{(1)}(T_R) \approx 0.017 \quad (48)$$

When air number densities were measured using a rotational line, Eq. (29) was used for data reduction. Therefore, an evaluation of the total uncertainty in  $C_{F2}(T)$  must be made using the relation

$$U[C_{F2}(T)] \approx \frac{U(T_R) T_R}{C_{F2}(T) \left( \frac{dT}{dC_{F2}(T)} \right)_{C_{F2}(T)}} \quad (49)$$

and evaluating Eq. (49) at  $T_R = 295 \text{ K}$  gives

$$U[C_{F2}(T)] \approx 0.008 \quad (50)$$

Combining the uncertainties in  $C_{F2}$  and  $C_{F2}(T)$  gives

$$B[C_{F2}, C_{F2}(T)] = \sqrt{\left\{ U[C_{F2}(T)] \right\}^2 + [U(C_{F2})]^2} \approx 0.021 \quad (51)$$

Therefore, using Eqs. (35) and (30) gives

$$U^{(1)}[n(\text{air})] \approx 0.0283 \quad (52)$$

For the tunnel calibration measurements a different laser power integrator was used, and the random error was measured to be

$$\sigma(E_o) = 0.0035 \quad (53)$$

Since  $\eta$  equals 1 for the tunnel calibration measurements, Eq. (31) gives

$$\sigma(N_m) = 0.0023 \quad (54)$$

The air number density measurements for the tunnel calibration experiments were presented as ratios of test section to stilling chamber number density. Furthermore, the two intensity values used were determined simultaneously; therefore, the error in  $E_0$  need not be considered. Thus the random errors in the intensity ratio were

$$S^{(2)}(I_m, \text{air}/\text{air}) = 0.0033 \quad (55)$$

The  $H_2O$  number density measurements for the tunnel calibration experiments were presented both in absolute terms and as a ratio to the air number density of the stilling chamber.

$$S^{(2)}(I_m, H_2O) = 0.025 \quad (56)$$

$$S^{(2)}(I_m, H_2O/\text{air}) = 0.025 \quad (57)$$

During the course of the tunnel calibration experiments, it was discovered that the test section windows were slowly fogging over during data runs, and this prevented reliance upon the air or  $H_2O$  calibration factors for data reduction. It should be noted that the initial experiments did not reveal any window fogging problems; however, the initial experiments were conducted in warm, summer weather, whereas the tunnel calibration experiments were conducted during some rather cold winter weather. Once the windows became initially fogged, the calibration factors for density became useless. However, continued window fogging was a very slow process; therefore, the numerical average of the measured values of density or density ratio taken during a particular data run was normalized to the average of the calculated values. Only random error is quoted for the tunnel calibration density measurements, since systematic error of calibrations was effectively eliminated, and the error due to the increasing fogging of the windows could not be estimated.

Because temperature measurements relied upon an intensity ratio determined from scattered light observed through the same test section view port, because of the closeness (12.8 Å) of the spectral lines monitored, and because of the relatively short time between intensity measurements, the temperature measurements were unaffected by the window fogging. Since the  $T_R$  measurements were conducted in essentially the same manner as were the initial experiments, the random error is evaluated as

$$S^{(2)}(R) = 0.0059 \quad (58)$$

and

$$U^{(2)}(R) = 0.0118 \quad (59)$$

Therefore, using Eq. (47) at  $T_R = 295$  K gives

$$U^{(2)}(T_R) = 0.0092 \quad (60)$$

As shown by Refs. 12, 13, and 14, fluctuations of measured parameters such as  $T_R$  and number density can introduce errors in time-averaged measurements of the parameters. The maximum rms fluctuation values estimated for ART are 2.4 percent for temperature and 3.7 percent for density. Using these values, the data reduction relations employed in this study, and the methods of Ref. 13, it was found that flow-field fluctuations contributed a negligible uncertainty to the measured values.

#### 4.3.2 Tunnel Data

The following quantities were calculated from the measured tunnel conditions for comparison with the Raman/Rayleigh scattering measurements:

1. Free-stream Mach number,  $M_\infty$
2. Free-stream static density of dry air,  $\rho_\infty(\text{air})$
3. Free-stream static temperature,  $T_\infty$
4. Static density and temperature profiles in the test section
5. Ratio of free-stream to stilling chamber static density,  $\rho_\infty/\rho_0$
6. Free-stream static density of water vapor,  $\rho_\infty(\text{H}_2\text{O})$
7. Ratio of free-stream water vapor to stilling chamber dry air static density,  $\rho_\infty(\text{H}_2\text{O})/\rho_{\infty,sc}(\text{air})$

For each of the calculated values, it was assumed that the flow was isentropic and the constituent gases were considered to be perfect gases. Therefore, the free-stream Mach number was calculated as

$$M_{\infty} = \left\{ \frac{2}{\gamma-1} \left[ \left( \frac{P_o}{P_{\infty}} \right)^{\frac{\gamma-1}{\gamma}} - 1 \right] \right\}^{\frac{1}{2}} \quad (61)$$

where  $P_o$  was the stagnation pressure of wet air measured in the stilling chamber,  $P_{\infty}$  was the free-stream static pressure of wet air measured in the test section, and  $\gamma$  was the ratio of specific heats (for air,  $\gamma = 1.4$ ).

From the measurement of total pressure and wet and dry bulb temperature, the stagnation pressure of dry air was calculated as

$$P_o \text{ (dry air)} = P_o \left( \frac{0.622}{\omega + 0.622} \right) \quad (62)$$

where  $\omega$  is the specific humidity corresponding to wet and dry bulb temperatures measured at the stagnation condition. A psychrometric chart from Ref. 15 was used to determine the values of  $\omega$  and the dewpoint of the air-water vapor mixture (note: the dewpoint temperature was affected very little by reduced pressure). The difference between the total pressure of wet and dry air on a typical summer day ( $\omega = 0.015$ ) was less than 2.5 percent.

Using the perfect gas law, the stagnation density of dry air was calculated as

$$\rho_o \text{ (dry air)} = \frac{P_o \text{ (dry air)}}{R \text{ (air)} T_o} \quad (63)$$

where  $R(\text{air})$  is the gas constant for air and  $T_o$  is the stagnation temperature. From the measurements of total and static pressure and the calculated stagnation density, Eq. (63), the free-stream static density of dry air was calculated by the isentropic flow relation, as follows:

$$\rho_{\infty} \text{ (dry air)} = \rho_o \text{ (dry air)} \left( \frac{P_{\infty}}{P_o} \right)^{1/\gamma} \quad (64)$$

The ratio  $P_{\infty}/P_o$  is the same at a given Mach number for dry or wet air as long as water vapor behaves as a perfect gas and no condensation occurs. Therefore, no correction was used to eliminate the contribution of water vapor to the total and static pressures. However, if 100-percent condensation were to occur between the stilling chamber and the test section, the uncertainty in the calculated value of static density would be increased by approximately 1.5 percent on a typical summer day.

The free-stream static temperature was calculated by the isentropic flow relation

$$T_{\infty} = T_o \left( \frac{P_{\infty}}{P_o} \right)^{\frac{\gamma-1}{\gamma}} \quad (65)$$

For the initial setup, the density and temperature profiles of the tunnel wall boundary layer were estimated using velocity profile data reported by Benek (Ref. 16). The modified Crocco relation

$$T = T_{wall} - (T_{aw} - T_{wall}) \frac{u}{u_{\infty}} - (T_{aw} - T_{\infty}) \left( \frac{u}{u_{\infty}} \right)^2 \quad (66)$$

was used to calculate the normalized temperature profile from the normalized velocity profile at adiabatic wall conditions ( $T_{wall} = T_{aw}$ ). At adiabatic wall conditions Eq. (66) reduces to

$$\frac{T}{T_{\infty}} = \frac{T_{aw}}{T_{\infty}} - \left( \frac{T_{aw}}{T_{\infty}} - 1 \right) \left( \frac{u}{u_{\infty}} \right)^2 \quad (67)$$

The ratio of the adiabatic wall temperature to the free-stream static temperature can be expressed in terms of free-stream Mach number as:

$$\frac{T_{aw}}{T_{\infty}} = 1 + r \left( \frac{\gamma-1}{2} \right) M_{\infty}^2 \quad (68)$$

where  $r$  is the temperature recovery factor that is approximately equal to 0.88 for a turbulent boundary layer. Substituting Eq. (68) into Eq. (67) yields

$$\frac{T}{T_{\infty}} = 1 + r \left( \frac{\gamma-1}{2} \right) M_{\infty}^2 \left[ 1 - \left( \frac{u}{u_{\infty}} \right)^2 \right] \quad (69)$$

Each value of  $u/u_{\infty}$  in the boundary-layer profile was substituted into Eq. (69) to calculate the normalized temperature profile.

The density profile was calculated from the temperature profile assuming constant static pressure through the boundary layer; therefore,

$$\frac{\rho}{\rho_{\infty}} = \frac{1}{(T/T_{\infty})} \quad (70)$$

The distributions of density and temperature in the boundary layer were determined by multiplying the normalized distributions obtained by Eqs. (69) and (70) by the appropriate free-stream values calculated by Eqs. (64) and (65).

During the tunnel calibration experiments, the ratio of stilling chamber static density to test section free-stream static density was calculated as follows:

$$\frac{\rho_{\infty}}{\rho_{\infty, sc}} = \left( \frac{P_{\infty}}{P_{\infty, sc}} \right)^{1/\gamma} \quad (71)$$

where the subscript sc refers to values measured in the stilling chamber and  $P_{\infty, sc}$  is the static pressure measured in the stilling chamber.

The free-stream water vapor density was calculated by determining the partial pressure of the water vapor at stagnation conditions and assuming that the vapor expanded isentropically, obeying the perfect gas law. Then,

$$\rho_{\infty} (H_2O) = \frac{P_o (H_2O)}{R (H_2O) T_o} \left( \frac{P_{\infty}}{P_o} \right)^{1/\gamma (H_2O)} \quad (72)$$

where

$$P_o (H_2O) = \frac{\omega}{0.622 + \omega} P_o$$

$$R (H_2O) = 85.76 \frac{\text{ft} \cdot \text{lbf}}{\text{lbm} \cdot ^\circ\text{R}}$$

$$\gamma (H_2O) = 1.329$$

As long as no condensation occurs, the composition of the air remains constant, and the ratio  $P_{\infty}/P_o$  is equal to the ratio  $P_{\infty} (H_2O)/P_o (H_2O)$ .

The ratio of the test section static density of water vapor to the stilling chamber static density of nitrogen was determined by dividing the density calculated in Eq. (72) by 0.7532 times the density calculated in Eq. (63), or

$$\frac{\rho_{\infty}(\text{H}_2\text{O})}{\rho_a(\text{N}_2)} = \frac{\rho_{\infty}(\text{H}_2\text{O})}{0.7532 \rho_a(\text{dry air})} \quad (73)$$

This assumes that the percentage of nitrogen in dry air is constant.

The uncertainties (combinations of systematic and random errors) of the basic tunnel parameters were established from repeated calibrations of the instrumentation and from the repeatability and uniformity of the test section flow during tunnel calibration. Uncertainties in the instrumentation systems were estimated from repeated calibrations of the systems against secondary standards whose uncertainties are traceable to the National Bureau of Standards calibration equipment. The instrument uncertainties were combined using the Taylor's series method of error propagation described in Ref. 17 to determine the uncertainties shown in Figs. 12 and 13 and in Table 1. The values quoted do not include possible measurement uncertainty in free-stream flow properties due to condensation of water vapor.

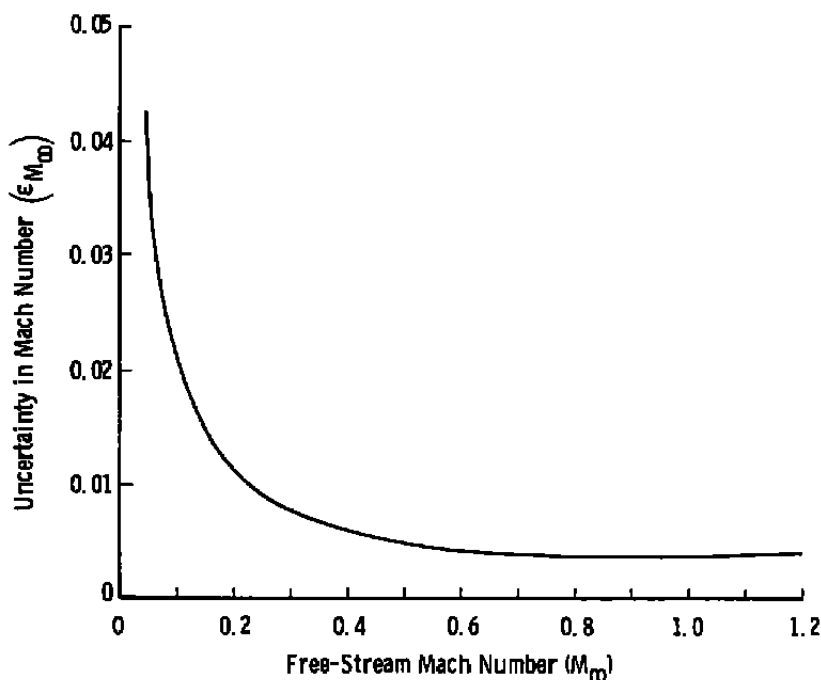


Figure 12. Uncertainty in free-stream Mach number.

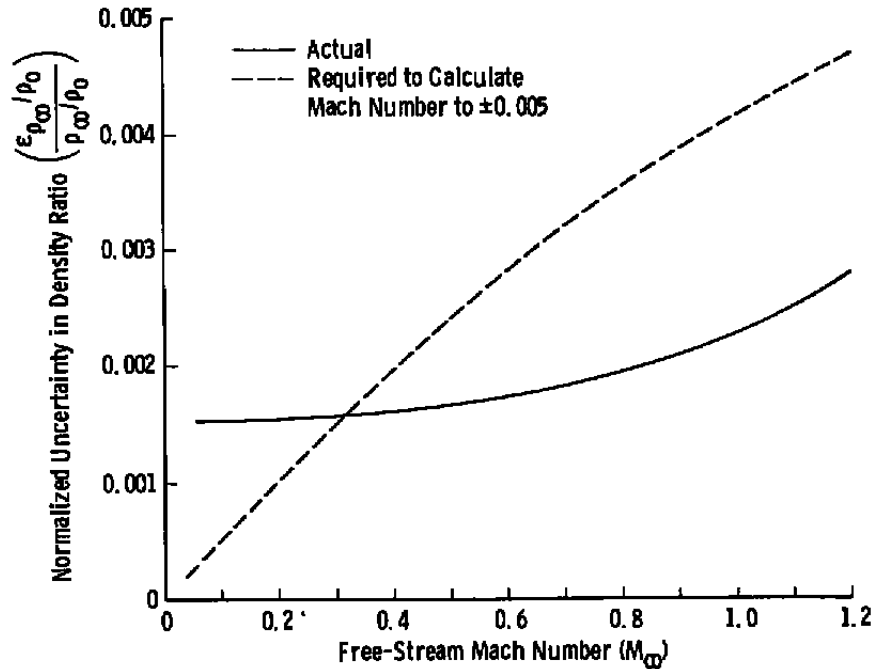


Figure 13. Uncertainty in density ratio as a function of Mach number.

Table 1. Uncertainties in Tunnel Parameters

<u>Parameter</u>	<u>Percent Uncertainty</u>
$p_o$ (Dry Air)	0.2
$\rho_o$ (Dry Air)	1.0
$\rho_\infty$ (Dry Air)	1.0
$T_\infty$	1.0
$\rho_\infty$ ( $H_2O$ )	7.0
$\rho_\infty$ ( $H_2O$ )/ $\rho_o$ ( $N_2$ )	7.0

Note: The uncertainties of these parameters were essentially constant for each Mach number and specific humidity encountered during the reported experiments.



## 5.0 PRESENTATION AND DISCUSSION OF EXPERIMENTAL RESULTS

### 5.1 NUMBER DENSITIES AND TEMPERATURES, AND RAYLEIGH SCATTERING RESULTS FROM THE INITIAL EXPERIMENTS

Results from the initial experiments are graphically presented in Figs. 14 through 20. Figure 14 is a vertical profile of the dry air density at Mach number 0.5. Density values are calculated from number density values with the following relation:

$$\rho \text{ (lbm/ft}^3\text{)} = 3.00 \times 10^{-21} n \text{ (air)} \quad (74)$$

Near the tunnel wall ( $y \leq 0.45$  in.) it can be seen that the measured values follow the calculated values within the estimated measurement uncertainty. It is believed that the larger variations of the measured values from the calculated curve from  $y = 0.5$  to  $2.75$  in. are a result of dirt collecting near the center portions of the laser beam entrance port and view port during the tunnel run. This theory is partly substantiated by the low data scatter in the  $\approx 0.4$ -in. scan region near the wall. The fairly rapid drop in density near the wall at  $y = 0.25$  in. is most interesting and is in considerable disagreement with the predicted value. A repeat scan during another test period again showed the rapid drop; furthermore, a scan at Mach number 0.8 revealed an even more rapid density drop near the wall. Although it was possible for the laser beam to be partially blocked near the wall, calibration scans for determination of  $T_F(y)$  did not reveal any beam blockage without any flow in the test section. It is quite significant for the Raman scattering technique that a data point could be taken within 0.025 in. of the wall. Data points even closer to the wall appear feasible with the use of a longer and narrower laser focal volume. No attempt was made to take data at distances within 0.025 inches of the wall because of the imprecision of the beam-positioning mechanism and the size of the laser beam focal volume.

Figure 15 is a vertical profile of the air rotational (static) temperature at Mach number 0.5 taken during a subsequent test period. The data agree very well with the predicted values within the estimated data uncertainty. Unfortunately, the data uncertainty ( $\pm 1.7$  percent) is still too large for an accurate study of the temperature boundary-layer profile. However, it is believed that the required data uncertainty (0.28 percent) can be obtained by simultaneously making the two intensity measurements needed for a temperature determination. This procedure would eliminate the need for making laser energy measurements and spectrometer wavelength adjustments. Use of an image intensifier/vidicon system and double exit slit assembly on the spectrometer can provide a method to make the simultaneous measurements. Such a system is under development at AEDC and was recently used for electron beam fluorescence measurements in a bipropellant rocket engine exhaust. A cruder version of such a system has been reported in Ref. 18.

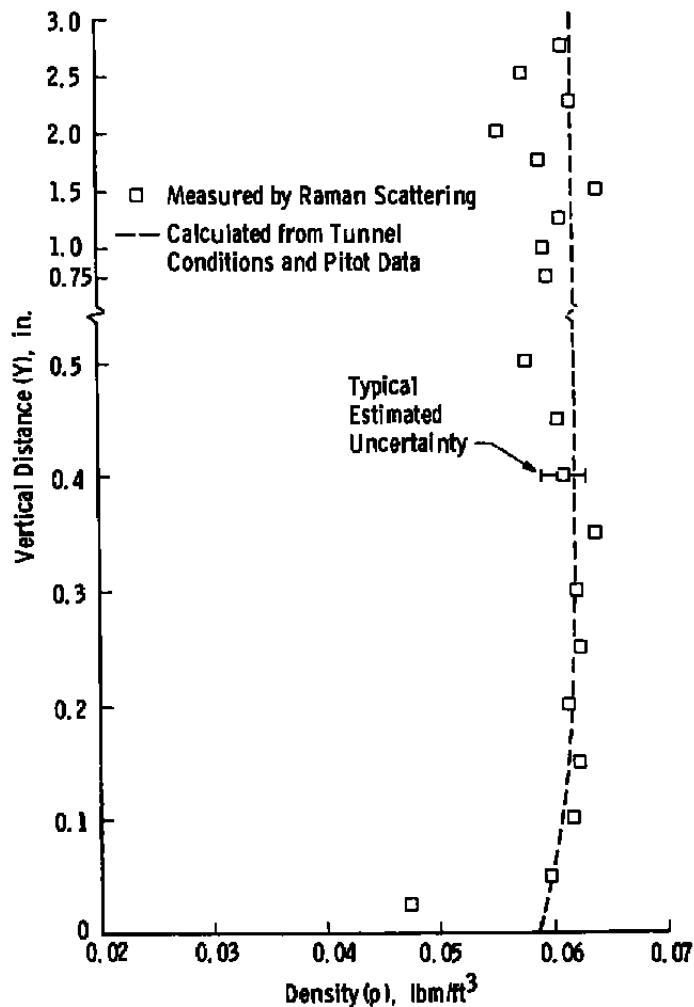


Figure 14. Density boundary-layer profile, Mach number 0.5, flat wall.

It is interesting to note that in the measured temperature profile the data scatter near the flow-field centerline is no larger than that observed near the wall; this contrasts with what was observed in the measured density profile. If, indeed, the major cause of the data scatter in the upper portion of the density profile was dirt on the optical ports, then the larger data scatter would not be present in the temperature measurements as a result of temperatures being determined from intensity ratios.

Figure 16 is a plot of air density as a function of Mach number at  $y = 2.5$  in. The measured and calculated values agree within the estimated measurement uncertainty. Again, the data uncertainty is larger than that required for transonic flow measurement to determine Mach number. However, elimination of the need to measure laser energy can improve the data uncertainty to the necessary level.

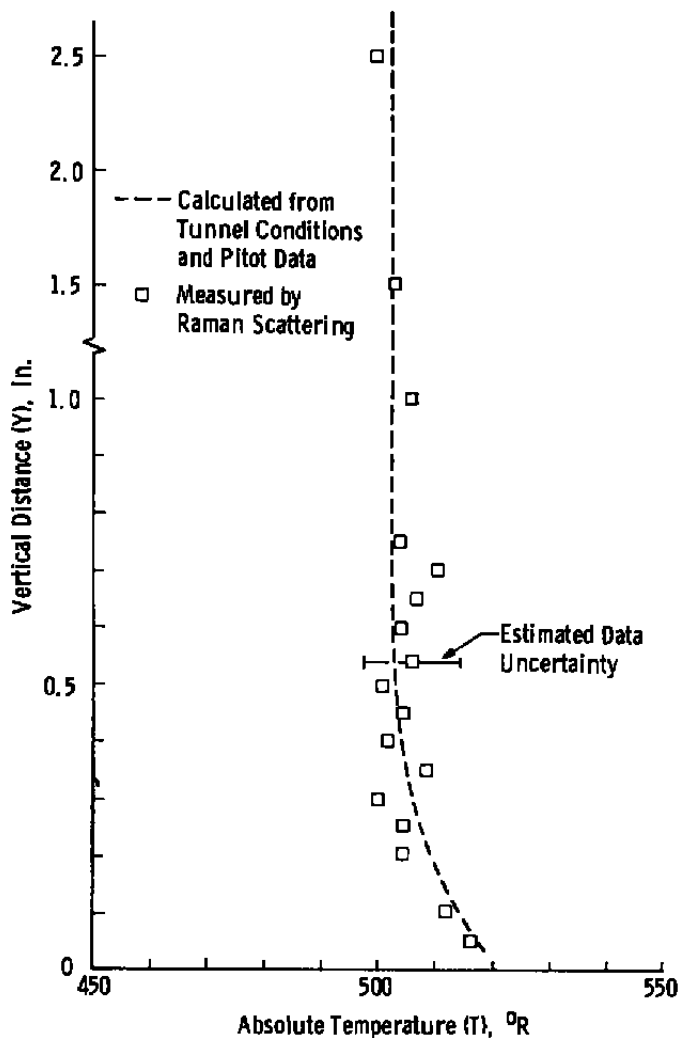


Figure 15. Static temperature boundary-layer profile, Mach number 0.5, flat wall.

Figure 17 is a plot of the air rotational (static) temperature as a function of Mach number at  $y = 2.5$  in. There is good agreement between measured and calculated values. While these temperatures were determined, an air density was simultaneously obtained. It was observed that the sensitivity of the detector had changed considerably from its value at the time of calibration; therefore, the Mach number 0.1 point was used to determine a density calibration factor. The resulting data plot is shown in Fig. 18. Figures 19 and 20 are also plots of static temperature and density, respectively, which are similar to Figs. 17 and 18 but were taken during a different test period.

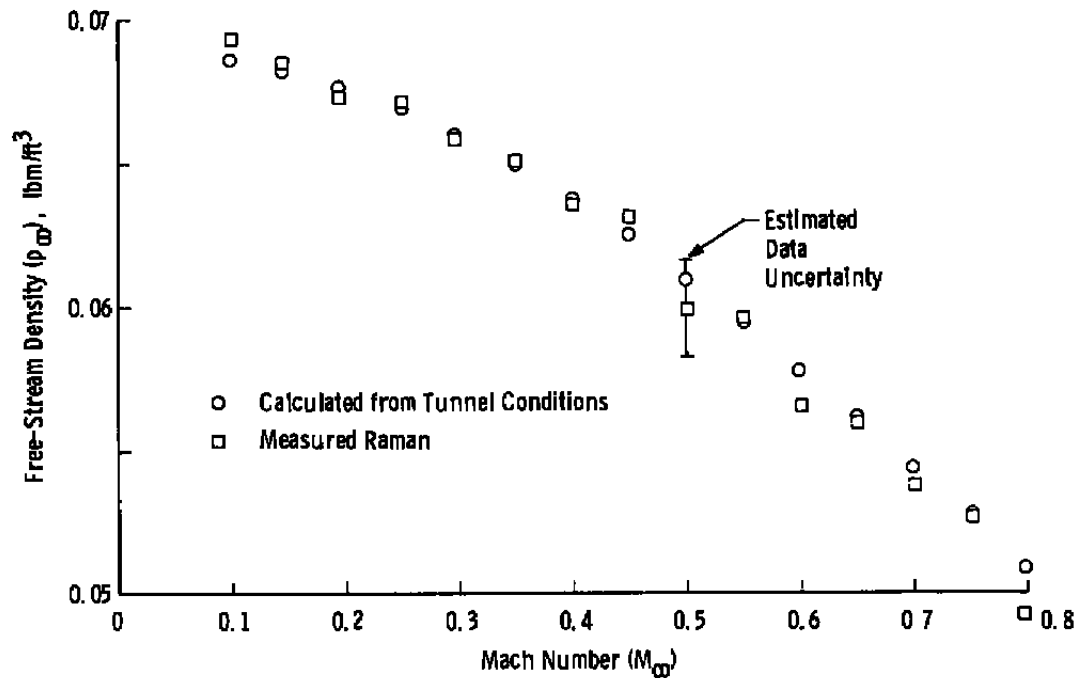


Figure 16. Free-stream density as a function of Mach number.

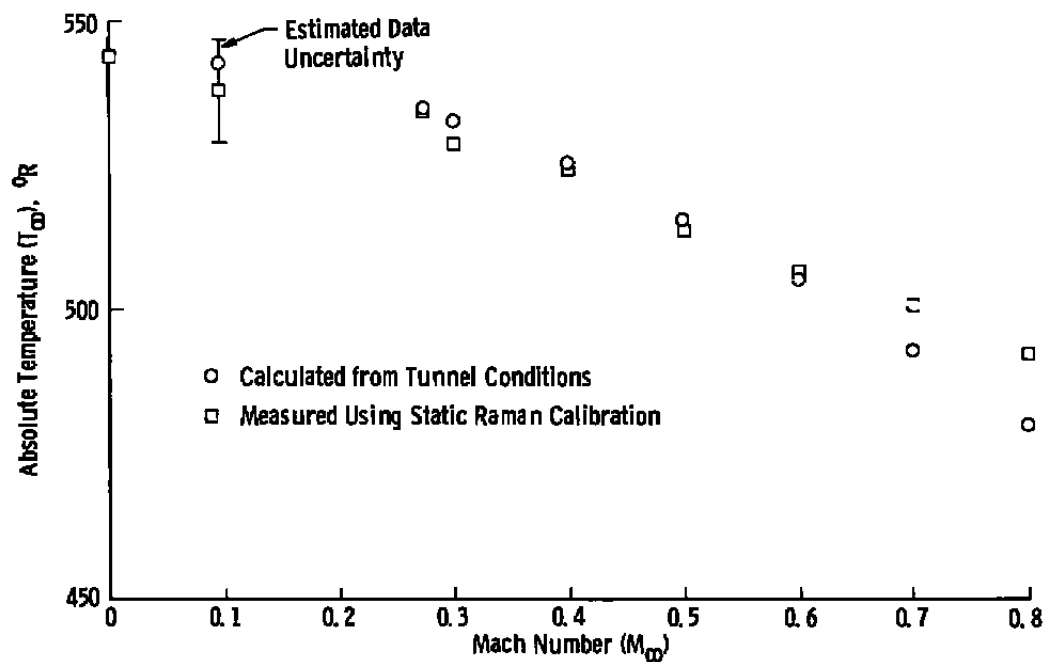


Figure 17. Free-stream static temperature as a function of Mach number.

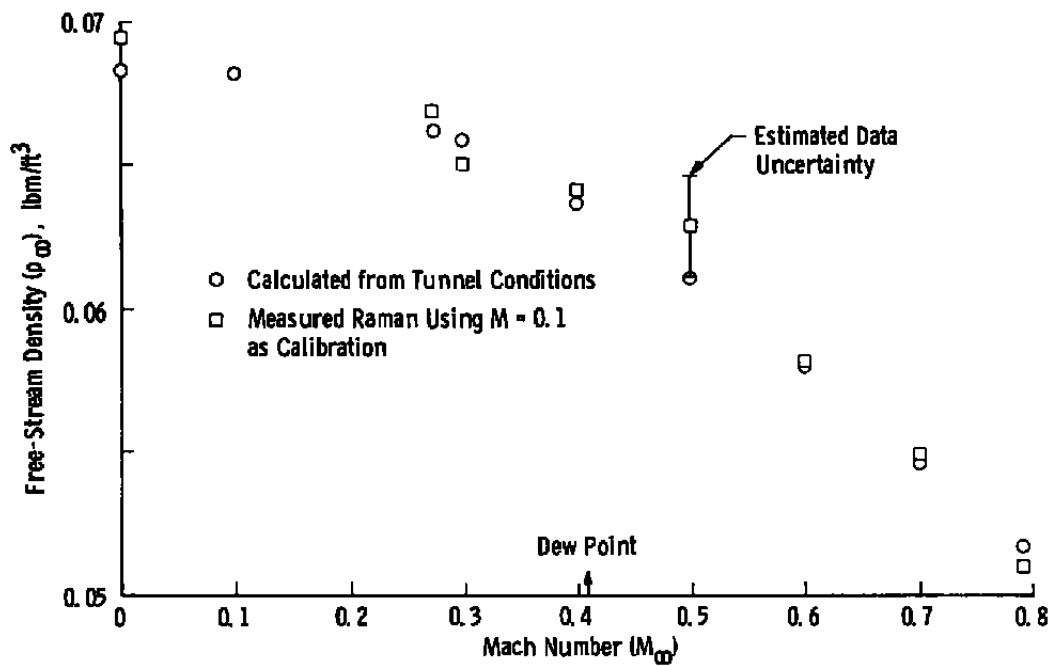


Figure 18. Free-stream density obtained during static temperature measurements as a function of Mach number.

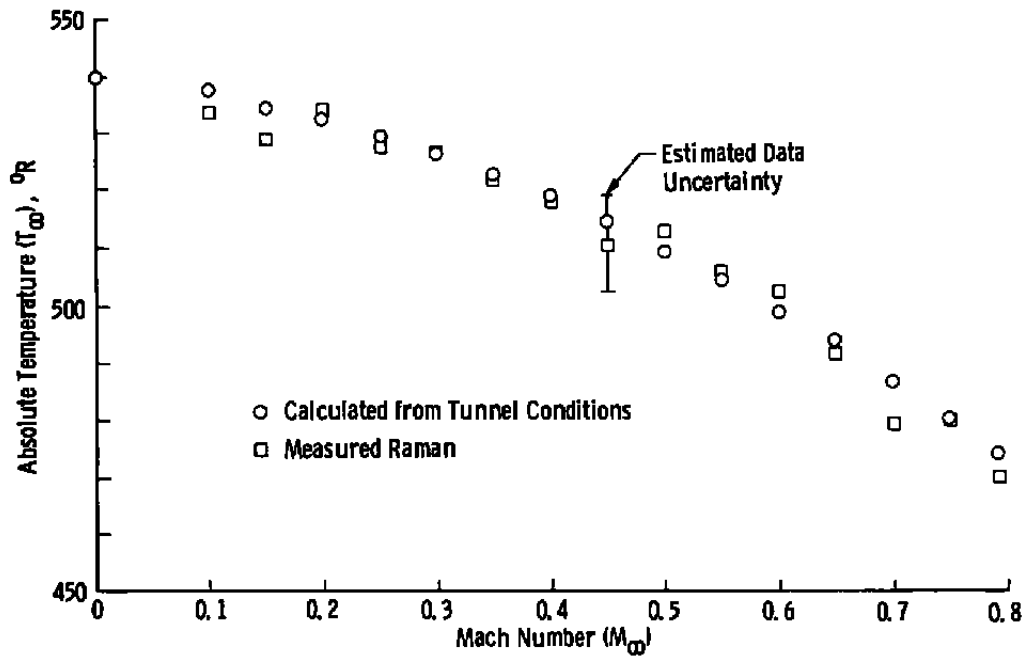


Figure 19. Free-stream static temperature as a function of Mach number, repeat.

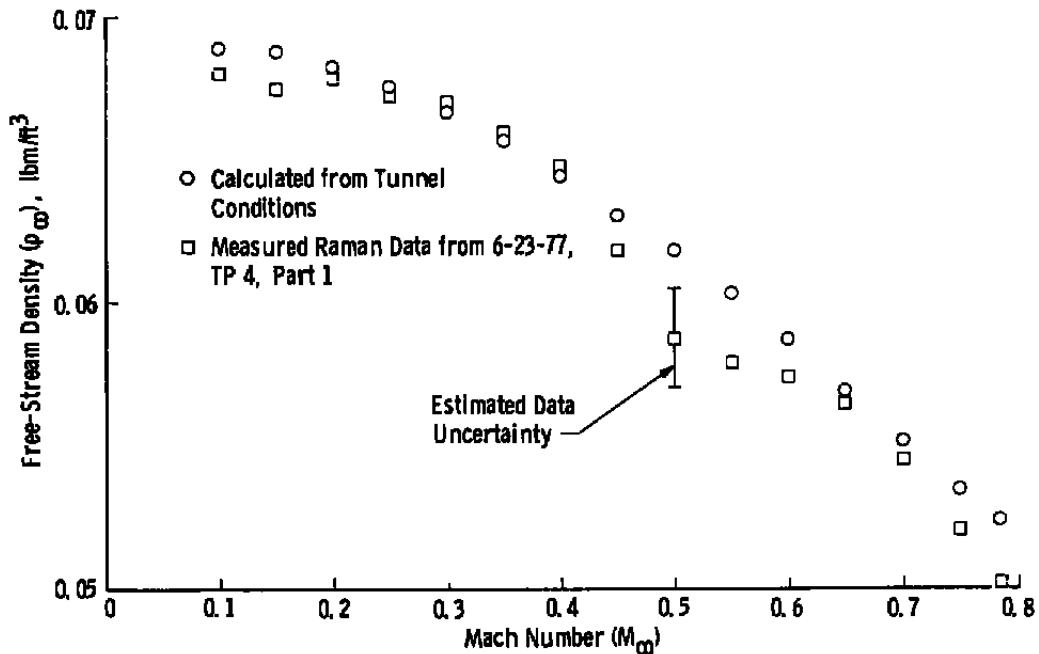


Figure 20. Free-stream density obtained during static temperature measurements as a function of Mach number, repeat.

Figure 21 is a plot of Rayleigh scattering data obtained during the initial experiments. Normalized Rayleigh scattering intensity polarized parallel to the polarization vector of the incident laser beam and depolarization ratio are plotted as functions of Mach number. Both normalized Rayleigh scattering intensity and depolarization ratio remain relatively steady up to Mach number 0.3. At this point the tunnel flow conditions are such that the dewpoint has been reached. It is interesting to note that condensation was not visible in the test section at this condition; in fact, visible condensation did not appear until the Mach number exceeded 0.65. As Mach number is increased further, the Rayleigh scattering intensity rises rapidly and the depolarization ratio drops rapidly. Both measured parameters have thus indicated the onset of  $H_2O$  condensation.

## 5.2 RESULTS FROM TUNNEL CALIBRATION EXPERIMENTS

Figures 22 through 26 are results obtained during the tunnel calibration experiments. Figures 22 and 23 are plots of the ratio of test section air number density to the stilling chamber air number density as a function of Mach number. Figure 23 shows the effect of the window fogging problem as Mach number increases, and at Mach number  $\approx 0.8$  an approximately 7-percent disagreement from the calculated value is seen. Figure 22 was prepared by fitting the average of the laser-Raman number density ratio measurements to

the average of the calculated values. The effect of the window fogging was thus minimized, and the good precision with which the measurements were made is demonstrated.

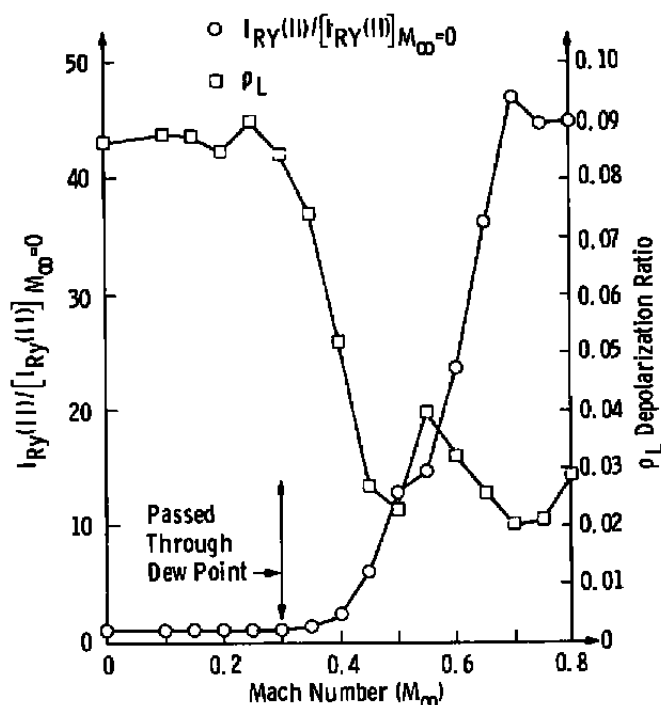


Figure 21. Test section Rayleigh scattering data as a function of Mach number,  $y = 2.5$  in.

Figure 24 is a plot of test section rotational (static) temperature as a function of Mach number, and excellent agreement between measured values and calculated values was obtained.

Figure 25 is a plot of  $H_2O$  density as a function of Mach number. The conversion of  $n(H_2O)$  to  $\rho(H_2O)$  is

$$\rho(H_2O), \text{lbm/ft}^3 = 1.87 \times 10^{-21} n(H_2O) \quad (75)$$

Within the estimated data precision there is good agreement between measured and calculated values. The major random error was the result of the low  $H_2O$  Raman signal level. The ratio of the  $H_2O$  density to the stilling chamber  $N_2$  density is also plotted as a function of Mach number in Fig. 26. The estimated data precision of 2.5 percent can be reduced to  $\approx 0.8$  percent by use of a filter system rather than a spectrometer system to detect the  $H_2O$  Raman signal.

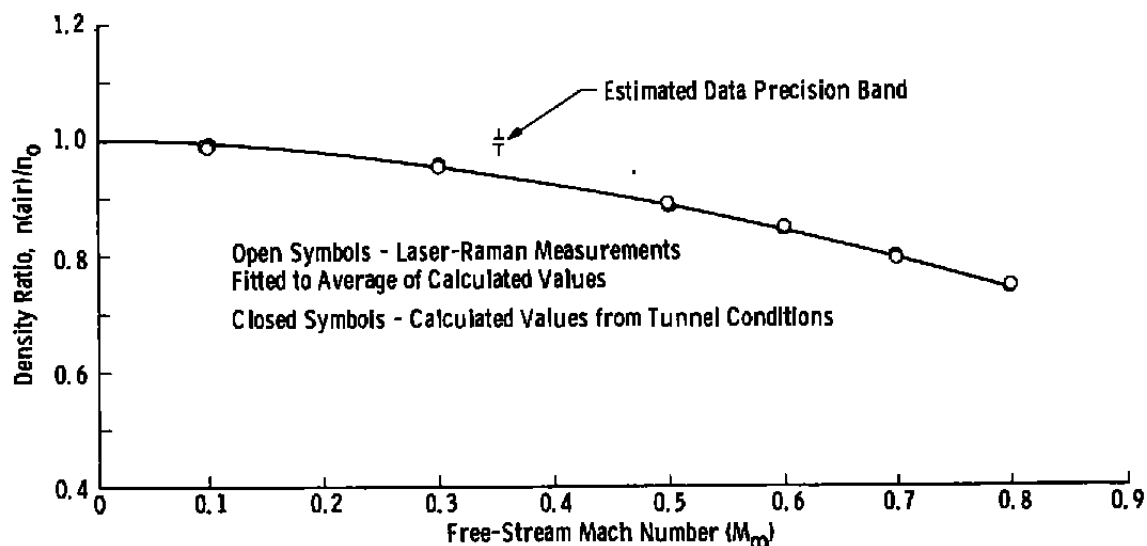


Figure 22. Ratio of test section and stilling chamber  $N_2$  number densities versus Mach number.

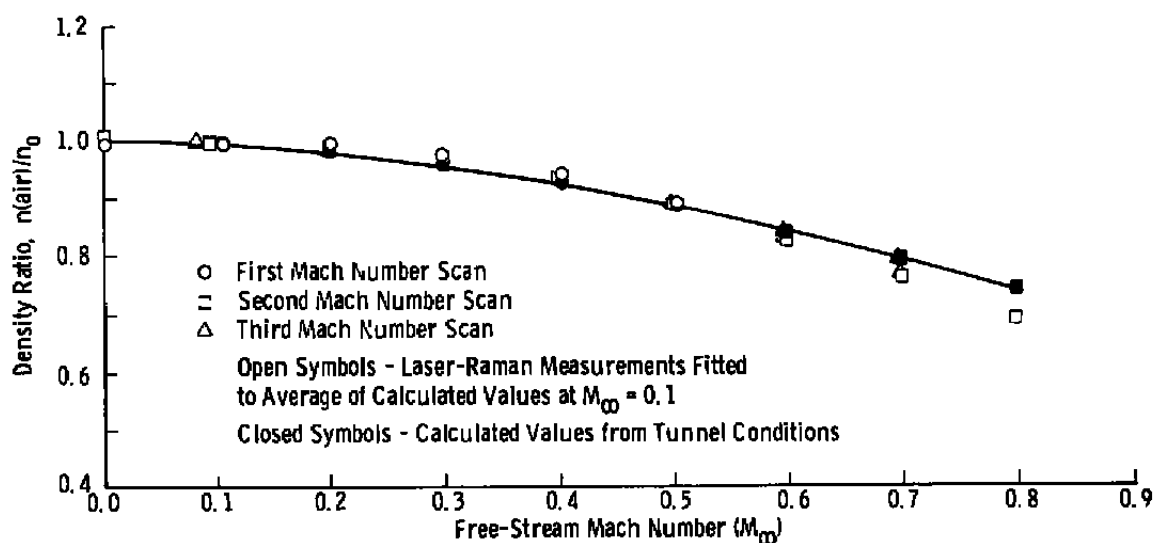


Figure 23. Ratio of test section and stilling chamber  $N_2$  number densities versus Mach number, repeat.



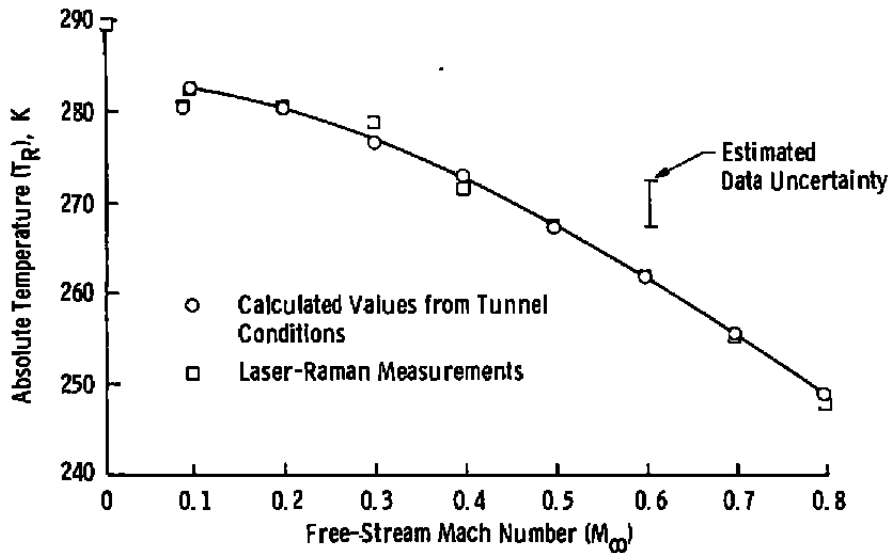


Figure 24. Free-stream static temperature as a function of Mach number, tunnel calibration experiment.

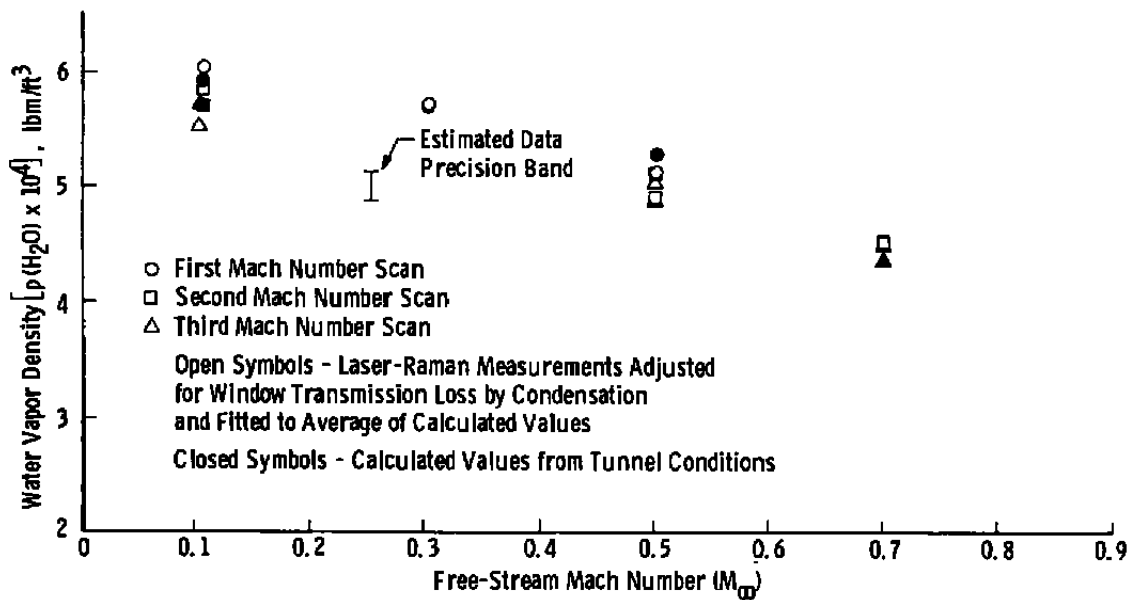


Figure 25. Free-stream  $H_2O$  density as a function of Mach number.

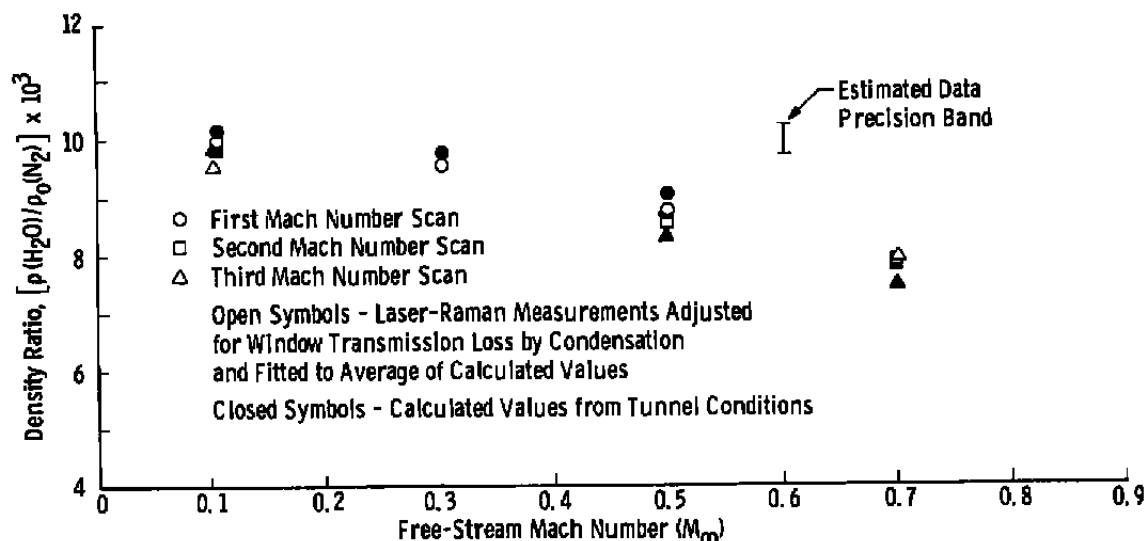


Figure 26. Ratio of test section  $H_2O$  density to stilling chamber  $N_2$  density as a function of Mach number.

## 6.0 CONCLUSIONS AND RECOMMENDATIONS

The following conclusions were reached from the Raman/Rayleigh scattering experiments performed in the Acoustic Research Tunnel (ART):

1. With the exception of boundary layers near the wall, static temperatures and air number density measurements were made which agree within estimated experimental uncertainty with predicted values. The measurements which did not agree were attributed to particulate matter adhering to the optical windows; however, the discrepancy near the wall is presently unexplainable and requires further study.
2. Measurements of temperature and air number density were made within 0.050 in. of the bottom wall of the test section, and it appears feasible to make measurements much closer to the wall with improved laser focusing and positioning apparatus. It also appears possible to make similar measurements around aerodynamic bodies in transonic flow.
3. The ability of the Raman scattering to measure  $H_2O$  number density in subsonic flow was demonstrated.
4. Rayleigh scattering was used to detect the onset of  $H_2O$  condensation, and the onset correlated very well with predicted dewpoint.

5. The feasibility of using the Raman/Rayleigh scattering technique for nonintrusive tunnel calibration was demonstrated. Improvements in the measurement technique such as increased laser power, elimination of window fogging effects, and use of the tunnel calibration experimental arrangement would increase the accuracy of the density measurements to the level where local Mach number could be specified to  $\pm 0.005$ .
6. The major experimental problem throughout these measurements was the collection of dirt and/or moisture on the optical ports of the ART. However, the window fogging problem would be avoided in a tunnel with humidity control and in larger tunnels where viewing holes would be used instead of windows.

The results of the experimental program in the ART suggest the following recommendations for improvements in the measurement technique and possible applications to current measurement problems:

1. For density measurements, optical filter systems should be used rather than a spectrometer system, to gain a factor of 5 to 10 in signal level.
2. For temperature measurements a spectrometer must be used, but a double slit/image intensifier/vidicon system can decrease measurement uncertainty by an order of magnitude.
3. Standard lamp light sources should be used to frequently check the relative sensitivities of the detectors employed.
4. Methods of eliminating the dirt and fogging of the viewing windows need to be studied. (One possible method: deep cavities with suction and heated ports.)
5. The capability of making nonintrusive measurements of local Mach number could be applied to the study of the effect of model blockage on wind tunnel calibration.
6. The ability to accurately monitor water vapor content and condensation could be used to correlate the effect of these parameters on aerodynamic coefficients. The response of the Raman/Rayleigh scattering technique to changes in water content is superior to the conventional method used at the present time in the AEDC Aerodynamic Wind Tunnel (4T) and Propulsion Wind Tunnel (16T).

## REFERENCES

1. Williams, W. D. and Lewis, J. W. L. "Rotational Temperature and Number Density Measurements of  $N_2$ ,  $O_2$ ,  $CO$ , and  $CO_2$  in a Hypersonic Flow Field Using Laser-Raman Spectroscopy." AEDC-TR-75-37 (AD-A012877), July 1975.
2. Lewis, J. W. L. and Williams, W. D. "Profile of an Anisentropic Nitrogen Nozzle Expansion." AEDC-TR-74-114 (AD-A004764), February 1975.
3. Jacocks, J. L. and Parker, R. L. "Suppression of Perforated Wall Noise in a Transonic Wind Tunnel and the Effects on Aerodynamic Data." AEDC-TR-78-20 (AD-A054417), May 1978.
4. Placzek, G. "Rayleigh and Raman Scattering." Translated from a publication of the Akademische Verlagsgesellschaft G. m. b. H., Leipzig, 1934, *Handbuch der Radiologie*, Heft 6, Teil 2, pp. 209-374.
5. Placzek, G. and Teller, E. "Die Rotationsstruktur der Ramanbanden Mehratomiger Molekule" ("Rotation Structure of the Raman Bands of Polyatomic Molecules"). *Zeitschrift fur Physik*, Vol. 31, March 1933.
6. Anderson, A., ed. *The Raman Effect, Vol. 2: Applications*. Marcel Dekker, Inc., New York, 1973.
7. Graham, S. C., Grant, A. J., and Jones, J. M. "Transient Molecular Concentration Measurements in Turbulent Flows Using Rayleigh Light Scattering." *AIAA Journal*, Vol. 12, No. 8, August 1974, pp. 1140-1142.
8. Bribes, J. L., Gaufres, R., Monan, M., Lapp, M., and Penney, C. M. "Raman Band Contours for Water Vapor as a Function of Temperature." *Applied Physics Letters*, Vol. 28, No. 6, 15 March 1976, pp. 336-337.
9. Williams, W. D. and Lewis, J. W. L. "Condensation Scaling Laws for Reservoir and Nozzle Parameters and Gas Species as Determined by Laser Scattering Experiments." AEDC-TR-76-67 (AD-A029733), September 1976.
10. Dougherty, N. S., Jr., Anderson, C. F., and Parker, R. L., Jr. "An Experimental Investigation of Techniques to Suppress Edgetones from Perforated Wind Tunnel Walls." AEDC-TR-75-88 (AD-A013728), August 1975.
11. Beers, Y. *Introduction to the Theory of Error*. Addison-Wesley Publishing Company, Inc., Reading, Massachusetts, 1953.

12. Lazdinis, S. S. "Effect of Fluctuations in Rotational Temperature, Vibrational Temperature, and Number Density on Time-Averaged Electron Beam Measurements of Nitrogen Rotational Temperature." AIAA Paper No. 75-180, presented at the 13th AIAA Aerospace Sciences Meeting, Pasadena, California, January 20-22, 1975.
13. Setchell, R. E. "Time-Averaged Measurements in Turbulent Flames Using Raman Spectroscopy." SAND-75-8695, January 1976.
14. Eckbreth, Alan C. "Averaging Considerations for Pulsed, Laser Raman Signals from Turbulent Combustion Media." *Combustion and Flame*, Vol. 31, No. 3, 1978, pp. 231-237.
15. Van Wylen, Gordon J. and Sonntag, Richard E. *Fundamentals of Classical Thermodynamics*. John Wiley and Sons, Inc., New York, 1968, p. 621.
16. Benek, J. A. "Effects of Acoustic and Vortical Disturbances on the Turbulent Boundary Layer at Free-Stream Mach Number 0.5." AEDC-TR-77-73 (AD-A047921), December 1977.
17. Holman, J. P. *Experimental Methods for Engineers*. McGraw-Hill Book Company, New York, 1971, pp. 33-78.
18. Black, Philip C. and Chang, Richard K. "Laser-Raman Optical Multichannel Analyzer for Transient Gas Concentration Profile and Temperature Determination." *AIAA Journal*, Vol. 16, No. 4, April 1978, pp. 295-296.

## NOMENCLATURE

a	Radius of Rayleigh scatterer, cm
ART	Acoustic Research Tunnel
B,B( )	Systematic error, fractional systematic error for the parameter in parentheses, respectively
C <sub>F</sub> (T)	A correction factor defined by Eq. (22) which accounts for differences between predicted and measured rotational line intensity at calibration conditions
C <sub>F</sub> (X)	Raman intensity density calibration factor for a species X, (molecules • counts)/(cm <sup>3</sup> • volts)
C <sub>F2</sub>	Density calibration factor for Raman intensity of the combined N <sub>2</sub> and O <sub>2</sub> rotational lines in air at 5160.9 Å, (molecules • counts)/(cm <sup>3</sup> • volts)

$C_{F2}(T)$	A temperature-dependent correction factor to account for the variation with temperature of the combined $N_2$ and $O_2$ rotational lines in air at 5,160.9 Å
$C_{FRy}, C_{FRy}^0$	Proportionality constant in Eqs. (1) and (10), respectively, with units of cm
$C_J$	A rotational quantum number-dependent parameter
$dC_{F2}(T)/dT$	Slope of the $C_{F2}(T)$ versus $T_R$ curve (see Fig. 9a)
$dR/dT$	Slope of the $R$ versus $T_R$ curve (see Fig. 9a)
$E_0$	Laser energy or time-integrated laser power, Joules or volts
$h$	Planck's constant, erg • sec
$I$	Intensity of the combined $N_2$ and $O_2$ rotational Raman lines in air, counts/volt
$I(H_2O, \nu_1)$	Intensity of the $H_2O$ $\nu_1$ vibration-rotation Raman band, counts/volt
$I(J, X)$	Intensity of the $J$ th rotational Raman line of species $X$ , counts/volt
$I(N_2, Q)$	Intensity of the $N_2$ vibration-rotation Raman band $Q$ branch, counts/volt
$I_{Ry}; I_{Ry}(\parallel), I_{Ry}(\perp)$	Rayleigh scattering intensity; Rayleigh scattering intensity polarized parallel and perpendicular to the polarization vector of the incident laser beam, respectively
$J$	Rotational quantum number
$M_\infty$	Free-stream Mach Number
$MPS$	Microprocessor system
$m$	Index of refraction of Rayleigh scatterer
$N_m$	Background-corrected photon counts accumulated during time interval $\tau$
$N(\tau)$	Photon counts accumulated during time interval $\tau$
$n_i, n$	Number density of $i$ th species, total number density of a gas mixture, molecules/cm <sup>3</sup>

$n_o$	Air number density in stilling chamber, molecules/cm <sup>3</sup>
$n(X)$	Number density of species X, molecules/cm <sup>3</sup>
$P, P(X)$	Static pressure and static pressure of species X, respectively, torr
$P_o(X)$	Stagnation pressure of gas X, psf
$P_s(H_2O)$	Saturation vapor pressure of H <sub>2</sub> O, torr
$P_\infty(X)$	Free-stream static pressure of gas X, psf
$q_R$	Rotational partition function
$R$	Ratio of combined N <sub>2</sub> and O <sub>2</sub> rotational line intensities at 5173.7 Å to those at 5160.9 Å
$RH$	Relative humidity
$R(X)$	Gas constant of gas X, ft-lbf/lbm °R
$r$	Temperature recovery factor (for air = 0.88)
$S, S( )$	Random error, fractional random error of parameter in parentheses
$T, T_R$	Static temperature, rotational temperature, Kelvins or degrees Rankine
$T_F(y)$	A correction factor to account for optical transmission differences in laser input and viewing ports
$T_o$	Stagnation temperature, °K or °R
$T_\infty$	Free-stream static temperature, °K or °R
$t$	Time
$U, U( )$	Total measurement uncertainty, fractional total uncertainty of parameter in parentheses
$u/u_\infty$	Boundary-layer velocity ratio
$X_i; X$	ith species of a gas mixture; indicates the species N <sub>2</sub> , H <sub>2</sub> O, or air
$y$	Vertical distance from bottom wall of ART test section, in.
$\alpha_i$	Polarizability of the ith species of a gas mixture, cm <sup>3</sup>
$\gamma, \gamma(H_2O)$	Ratio of specific heats for air or water vapor

$\Delta T, \Delta R$	Variation in temperature and intensity ratio, respectively
$\eta$	Ratio of the time duration for accumulating signal counts to the time duration for accumulating background counts
$\Theta_x$	Characteristic rotational temperature of species X, Kelvins
$\lambda_0$	Wavelength of the incident laser beam, cm or Å
$\nu_0$	Frequency of the incident laser beam, Hz
$\nu_1$	Vibration-rotation band designation for H <sub>2</sub> O
$Q_L$	Rayleigh scattering depolarization ratio
$\rho(X)$	Density of species X, lbm/ft <sup>3</sup>
$\sigma_i$	Rayleigh scattering cross section of the ith species of a gas mixture
$\sigma( )$	Fractional standard deviation of the parameter in parentheses
$\tau$	Time interval, sec
$\omega$	Specific humidity of air, lbm H <sub>2</sub> O/lbm dry air

#### Superscripts

(1)	Indicates measurement value determined during initial experiments
(2)	Indicates measurement value determined during tunnel calibration experiments
o	Indicates a calibration value
t	Indicates a test condition value

#### Subscripts

1,2	Indicates the combined rotational lines at 5,173.7 Å and 5,160.0 Å, respectively
aw	Adiabatic wall condition
B	Indicates a background measurement
c	Indicates a calculated value
d	Indicates a moisture-free value



<b>i</b>	Indicates the <i>i</i> th species of a gas mixture
<b>m</b>	Indicates a measured value
<b>o</b>	Stagnation values
<b>s</b>	Indicates a signal measurement
<b>sc</b>	Condition measured in stilling chamber
<b>WALL</b>	Value measured at the wall
<b>w</b>	Indicates a value including moisture
<b>∞</b>	Free-stream values